Deciphering the molecular mechanism of DNA-protein interactive co-condensates

Cheng Li[1, †], Yunqiang Bian[2, †], Yiting Tang[3, †], Lingyu Meng[1], Peipei Yin[1, 7], Ye Hong[4, 8], Jun Cheng[1], Yuchen Li[1], Jie Lin[1], Chao Tang[1, 5], Chunlai Chen[3, *], Wenfei Li[2, 6, *], and Zhi Qi[1, *]

[†]Equal contribution

[1]Center for Quantitative Biology, Peking-Tsinghua Center for Life Sciences, Academy for Advanced Interdisciplinary Studies, Peking University, Beijing 100871, China

[2]Wenzhou Key Laboratory of Biophysics, Wenzhou Institute, University of Chinese Academy of Sciences, Wenzhou, Zhejiang 325000, China

[3]School of Life Sciences, Beijing Advanced Innovation Center for Structural Biology, Beijing Frontier Research Center for Biological Structure, State Key Laboratory of Membrane Biology, Tsinghua University, 100084 Beijing, China

[4]The Integrated Science Program, Yuanpei College, Peking University, Beijing 100871, China

[5]School of Physics, Peking University, Beijing 100871, China

[6]Department of Physics, National Laboratory of Solid-State Microstructure, and Collaborative Innovation Center of Advanced Microstructures, Nanjing University, Nanjing 210093, China

[7]Present address: College of Life Sciences, Beijing Normal University, Beijing 100875, China

[8]Present address: School of Life Sciences, Tsinghua University, 100084 Beijing, China

*To whom correspondence should be addressed: zhiqi7@pku.edu.edu; wfli@nju.edu.cn; chunlai@mail.tsinghua.edu.cn

Abstract

Double-stranded DNA (dsDNA)-protein co-condensates (DPCs) play a crucial role in various fundamental cellular processes. Despite their significance, the molecular mechanisms governing DPCs remain elusive. To address this gap, we employed dsDNA and the transcription factor (TF) p53 as a model system to investigate a special case—dsDNA-protein interactive co-condensates (DPICs), where neither dsDNA nor the protein demonstrates phase-separation capacity. Through a combination of diverse experimental assays and theoretical methodologies, our investigation reveals that p53 acts as a bridge between different DNA duplexes, facilitating the DPIC formation. Using atomic force microscopy-based force spectroscopy (AFM-FS), we measured the viscoelastic properties of these DPICs. Additionally, we analyzed the phase diagram of DPICs, uncovering two distinctive transition behaviors: a phase transition between viscoelastic fluid and viscoelastic solid, and a morphology transition between DPICs with droplet-like morphology and “pearl chain”-like structure. Finally, we established the relationship between DNA-protein interaction strength, relaxation time, and condensate morphology.

Introduction

Eukaryotic cells utilize lipid membranes to compartmentalize intracellular organization. However, recent advancements in *in vivo* and *in vitro* research have unveiled an alternative mechanism employed by these cells to organize their complex biochemistry (Alberti, 2017). Specifically, macromolecules, such as nucleic acids and proteins, have been identified to undergo liquid-liquid phase separation (LLPS), leading to the assembly of membrane-lacking compartments (Alberti and Dormann, 2019; Banani et al., 2017; Berry et al., 2018; Boeynaems et al., 2018; Shin and Brangwynne, 2017). Two primary driving forces for the formation of LLPS include protein intrinsically disordered regions (IDRs) (Uversky, 2017) and/or multivalent interactions among modular biomacromolecules (Li et al., 2012). These membrane-lacking compartments are recognized as biomolecular condensates, playing pivotal roles in various biological functions. Importantly, the dysregulation of condensation processes has been implicated in a spectrum of human diseases (Alberti and Dormann, 2019).

Biomolecular condensates, arising from individual or multiple biomacromolecular species, manifest as either single-component or multi-component entities. Notably, nucleic acids have emerged as pivotal scaffolds, orchestrating the formation of nucleic acid-protein co-condensates, a distinct subclass of two-component condensates (Feric and Misteli, 2022). For example, RNA-protein co-condensates (RPCs) have been studied very well (Alshareedah et al., 2019; Alshareedah et al., 2021; Alshareedah et al., 2022; Boeynaems et al., 2019; Lin et al., 2015; Zhang et al., 2015).

In addition to RPCs, considerable attention has been directed towards comprehending double-stranded DNA (dsDNA)-protein co-condensates (DPCs). An in-depth

understanding of the molecular mechanisms governing DPCs is imperative for unraveling essential cellular processes, including chromatin formation (Gibson et al., 2019; Hansen et al., 2021; Larson et al., 2017; Li et al., 2020; Strickfaden et al., 2020; Strom et al., 2017; Wang et al., 2019; Wang et al., 2020) and the formation of transcription initiation condensates (Boija et al., 2018; Cho et al., 2018; Chong et al., 2018; Sabari et al., 2018; Zuo et al., 2021).

In our pursuit of a deeper understanding of DPCs, we initially explore a simplified version where neither the dsDNA nor the protein exhibits phase-separation capacity. Remarkably, the combination of these components gives rise to co-condensates, a phenomenon termed dsDNA-protein interactive co-condensates (DPICs) (Erdel and Rippe, 2018). Numerous proteins, such as cyclic GMP-AMP synthase (cGAS) (Du and Chen, 2018), Vernalization 1 (VRN1) (Zhou et al., 2019), transcription factor (TF) FoxA1 (Quail et al., 2021), the DNA-binding domains (DBDs) of reprogramming factor Krüppel like factor 4 (KLF4) (Sharma et al., 2021), and Kaposi's sarcoma-associated herpesvirus (KSHV) ORF52 (Xu et al., 2021), have been identified as capable of forming DPICs with DNA.

While several investigations have delved into DPICs, the fundamental biophysical characteristics of dsDNA in conjunction with proteins within DPICs unclear and questions remain. For example, how do interaction strengths between dsDNA and protein regulate the DPICs? How is the DPIC structure organized? Additionally, what are the material properties and condensate morphology of the DPICs? To address these uncertainties and decipher the underlying physical parameters steering DPIC formation, we employ a combination of experimental and theoretical methodologies.

We selected p53 as our model system, given its prominence as one of the most extensively studied human TFs, owing to its key role in safeguarding against tumorigenesis in eukaryotic cells (Hafner et al., 2019). p53 assembles into a tetramer consisting of two dimers. Each monomer contains an amino-terminal transactivation domain (TAD, 1-62), a proline-rich domain (PRD, 63-94), a sequence-specific, highly-conserved core DBD (95-292), a short intrinsically disordered hinge domain (HD, 293-324), an oligomerization domain (OD, 325-356), and a carboxyl-terminal domain (CTD, 357-393) (Sullivan et al., 2018) (Fig. 1a(i)). Both the core DBD and CTD, possess DNA-binding capabilities. The CTD is responsible for nonspecific DNA searching, while the core DBD selectively binds to p53-binding motifs (McKinney et al., 2004; Tafvizi et al., 2011). p53 recognizes specific binding motifs, approximately 20 base pair (bp) DNA sequences containing two 10-bp half-site sequences. Each dimer within the p53 tetramer binds to one half-site sequence. The interaction of p53 with its target sequences brings about substantial alterations in downstream gene transcription, exerting a significant impact on cellular functions. For instance, binding to the p21 binding site, a crucial p53-binding motif, can induce cell cycle arrest (Hafner *et al.*, 2019; Wei et al., 2006). The interactions between DNA and p53 are finely regulated, rendering p53 an exemplary candidate for unraveling the molecular mechanisms underlying DPICs.

This study reveals that in the absence of the TAD, the p53 mutant, $p53^{4M}$ ΔTAD, possesses the capability to form DPICs with dsDNA. Molecular dynamics (MD) simulations provide insight into the mechanism of DPIC formation, attributing it to the bridging capacity of p53 between different DNA molecules. Increasing the number of bridges on each DNA or the binding affinity between DNA and protein induces a

morphological transition from a droplet-like to a “pearl chain”-like structure. Using atomic force microscopy-based force spectroscopy (AFM-FS), we confirm the viscoelastic properties of these DPICs. Additionally, we meticulously delineate the phase diagram of DPICs, uncovering two distinctive transition behaviors: a phase transition between viscoelastic fluid and viscoelastic solid, and a morphology transition between DPICs with droplet-like morphology and those exhibiting a “pearl chain”-like structure. We further established the relationship between DNA-protein interaction strength, relaxation time, and condensate morphology. Based on well-established principles in soft matter physics, we construct a theoretical model to elucidate the molecular mechanisms governing DPICs.

Results

$p53^{4M}$ ΔTAD can form droplet-like DPICs with random dsDNA

While wild-type (WT) human p53 (Fig. 1a(i)) exhibits susceptibility to *in vitro* degradation, the Fersht lab has identified a variant with enhanced thermodynamic stability through the substitution of four residues (M133L/V203A/N239Y/N268D) in the DNA-binding domain (DBD) – $p53^{4M}$ (Fig. 1a(ii)) (Nikolova et al., 1998). Consequently, we undertook the *in vitro* purification of $p53^{4M}$ (Supplementary Fig. 1a and **Methods**). Experimental validation of its activity was conducted through two distinct assays: electrophoretic mobility shift assays (EMSAs) (Supplementary Fig. 1b) and luciferase assays (Supplementary Fig. 1c). In *in vitro* droplet assays conducted under physiological conditions (8 mM Tris-HCl (pH 7.5) and 120 mM NaCl), co-condensate formation was not observed for 40 μM $p53^{4M}$ in combination with 0.9 μM 400-bp DNA substrates containing non-specific sequences

(random DNA) (Supplementary Fig. 1d). However, upon removal of the TAD ($p53^{4M}$ ΔTAD, Supplementary Fig. 2a-b), 20 μM $p53^{4M}$ ΔTAD demonstrated the capability to induce droplet-like DPIC formation when mixed with 0.6 μM 400-bp random DNA (Fig. 1b and Supplementary Movie 1). To scrutinize the intricate details of DPICs, we conducted *in vitro* droplet assays, systematically combining concentrations of 0, 0.15, 0.3, 0.6, and 0.9 μM 400-bp random DNA labeled with DAPI with 0, 2.5, 5, 10, 20, and 40 μM dark $p53^{4M}$ ΔTAD, thereby constructing a phase diagram (Fig. 1c). Our findings indicate that neither 0.9 μM DNA nor 40 μM protein in isolation undergoes LLPS, confirming the distinctive nature of our co-condensates as DPICs. Therefore, we chose $p53^{4M}$ ΔTAD as a biophysical model in this study to quantitatively explore the molecular mechanisms underlying DPICs. It is imperative to note that, despite the significant biological relevance of the human TF p53, this work confines its focus to considering $p53^{4M}$ ΔTAD as an ideal candidate for a thorough exploration of the quantitative biophysical mechanisms governing DPICs. It is pertinent to mention that the working buffer employed in our experiments does not contain crowding agents. Furthermore, the concentration of p53 referred to henceforth pertains to the monomeric concentration. In all instances during the *in vitro* droplet assays, samples were thoroughly mixed and incubated for a duration of 30 minutes prior to data acquisition, unless specified otherwise.

Remarkably, the droplet-like DPICs exhibited an intriguingly slow fusion kinetics (>150 seconds in Fig. 1d. In stark contrast, conventional one-component liquid condensates, exemplified by hnRNPA1 condensates, typically undergo complete fusion within approximately 3 seconds (Molliex et al., 2015). To gain deeper insights into the prolonged fusion process, a two-color experiment was conducted (Fig. 1e(i)). Initially, 20 μM dark

p53^{4M} ΔTAD was mixed with 0.6 μM 400-bp random DNA labeled by FAM, resulting in the formation of initial green DPICs. Subsequently, the buffer was exchanged with a fresh solution containing 20 μM p53^{4M} ΔTAD labeled by ATTO565 and 0.6 μM dark 400-bp random DNA. The ensuing 1-hour dynamic fusion process was observed in Fig. 1e(ii)-(iii). Notably, many red droplet-like DPICs underwent coalescence with green counterparts, establishing a distinct boundary during the fusion process. This two-color experiment conclusively verified the inability of the protein within red DPICs and the DNA within the green DPICs to mix well, emphasizing a pronounced material specificity of DPICs, which will be discussed in more detail in the following subsection.

We also conducted fluorescence recovery after photobleaching (FRAP) experiments (**Methods** and Supplementary Fig. 3) for 0.6 μM 400-bp random DNA labeled with FAM mixed with 20 μM p53^{4M} ΔTAD labeled with ATTO565 (Fig. 1f(i)). The FRAP analysis revealed a slow yet substantial recovery for p53^{4M} ΔTAD (depicted by the red curve in Fig. 1f(ii)). In parallel, the FAM-labeled random DNA exhibited a more limited recovery (illustrated by the green curve in Fig. 1f(ii)). These FRAP results robustly suggest that DNA serves as the structural framework, constituting the skeleton of DPIC, while the protein functions as the connecting joint within the DPIC framework.

To fully understand the biophysical nature of these droplet-like DPICs, we mixed 40 μM p53^{4M} ΔTAD with 0.6 μM 400-bp random DNA in a physiological buffer containing 120 mM NaCl (Fig. 1g(i)). Upon increasing the NaCl concentration to 500 mM, a noteworthy phenomenon unfolded—many DPICs dissipated within a brief 5-minute interval (Fig. 1g(ii)), and subsequent restoration was observed upon decreasing NaCl concentration back to 120 mM, albeit requiring a duration of 30 to 60 minutes (Fig. 1g(iii)). Furthermore,

the impact of 1,6-hexanediol (1,6-HD) presence was examined, revealing that DPICs did not undergo disassembly even in the presence of 10% 1,6-HD (Fig. 1h). These findings robustly indicate that the DPICs are driven largely by electrostatic interactions between DNA and $p53^{4M}$ ΔTAD, as opposed to hydrophobic interactions.

The capacity of p53 to bridge different DNA duplexes induces the DPIC formation

Our subsequent inquiry delved into the microscopic architecture of the DPIC. Previous study (Sharma *et al.*, 2021) has demonstrated that the DBDs of KLF4 is proficient in forming DPICs with DNA, simultaneously exhibiting a special capability to bridge diverse DNA duplexes. This finding underscores a potential crucial correlation between the DNA-bridging capacity of KLF4 DBD and the formation of DPICs. In a parallel line of evidence, previous investigations (Kearns et al., 2016) have revealed the ability of a p53 tetramer to bridge different DNA duplexes. Collectively, these observations led us to formulate a hypothesis positing that the capacity of p53 to bridge distinct DNA duplexes plays a pivotal role in inducing the formation of DPICs.

To support this idea, we conducted coarse-grained MD simulations using the 3SPN-AICG energy function (Freeman et al., 2014; Lequieu et al., 2017; Li et al., 2014; Li et al., 2011) to analyze the structural and interaction features of DNA and p53 within a DPIC (**Supplementary Methods**). In this coarse-grained molecular model, each amino acid is simplified as one spherical bead centered around its C_α position. Similarly, each nucleotide is represented by three beads corresponding to the phosphate, sugar, and base, respectively (Fig. 2a(i) and Supplementary Fig. 4a). The structure-based potential AICG2+ (Li *et al.*, 2014) was applied to the core DBD and OD domains in order to maintain

the structural stabilities of the folded domains and the tetrameric state of the p53^{4M} ΔTAD chains. The intrinsically disordered parts were modelled by using a statistical potential developed by Terakawa and Takada in a previous work (Terakawa and Takada, 2011), which has been demonstrated to be successful in reproducing the experimentally observed properties of the intrinsically disordered TAD domain of p53. Since p53 and DNA interact mainly through electrostatic interactions, we employed the Debye-Hückel model, which can reasonably describe the Coulombic screening effect of monovalent salt under different concentrations. All simulations were conducted with the GENESIS 1.7.1 package (Jung et al., 2015; Kobayashi et al., 2017; Tan et al., 2022) at a temperature of 300 K controlled by the Langevin dynamics. More details of the coarse-grained simulations can be found in **Supplementary Methods**. Such coarse-grained modeling enables us to simulate large-scale biomolecular processes over longer timescales that are otherwise inaccessible in an atomistic model.

We first conducted MD simulations for a system containing 7 random dsDNAs and 27 p53^{4M} ΔTAD tetramers (Fig. 2a(ii) and Supplementary Fig. 4b). Here the length of dsDNA was set as 199-bp in the simulations for simplicity, considering that the morphology of the DPICs does not change when the length of dsDNA increases from 199-bp to 400-bp (Supplementary Fig. 2c). This simulation began from an initial configuration in which all molecules were randomly positioned in a cubic box with rare inter-molecule bridging interactions (Supplementary Fig. 4b(i)). While the timescale of the MD simulation was still much shorter than an experimentally relevant timescale, one can observe that the DNA-p53 system gradually developed multivalent bridging interactions (Supplementary Fig.

4b(ii), c, and Supplementary Movie 2). Over time, one p53^{4M} ΔTAD tetramer has an opportunity to bind with multiple dsDNA chains, and vice versa.

The above system has a large number of degrees of freedom, and the conformational sampling in these molecular simulations is extremely slow, making quantitative analysis difficult. To more comprehensively and quantitatively characterize the effects of different factors on the capability of p53 tetramers to bridge multiple dsDNA chains, we performed extensive simulations on a much smaller system containing 2 p53^{4M} ΔTAD tetramers and 10 199-bp random dsDNA chains in a 150 mM salt concentration. This set of MD simulations was named as MD 1 (blue bars in Fig. 2c-d, and Supplementary Movie 3). In order to quantitatively characterize multivalent bridging interactions, we defined N_{DNA} to represent the number of different dsDNA chains that one p53^{4M} ΔTAD tetramer can bridge (**Supplementary Methods** and Fig. 2b). We obtained $N_{DNA} = 3.5 \pm 0.7$ (n = 3) for MD 1 (Supplementary Fig. 5a(i)), indicating that each p53^{4M} ΔTAD tetramer is able to bridge multiple different dsDNA chains. Similar results were obtained when the number of p53^{4M} ΔTAD tetramers and dsDNA chains were altered within a reasonable range (Supplementary Fig. 5b). For comparison, we also performed two additional sets of simulations: (*i*) MD 2: 2 full-length p53^{4M} tetramers and 10 199-bp random dsDNA chains in a 150 mM salt concentration, $N_{DNA} = 2.0 \pm 0.9$ (n = 3) (green bars in Fig. 2c, Supplementary Fig. 5a(ii), and Supplementary Movie 4); (*ii*) MD 3: 2 p53^{4M} ΔTAD tetramers and 10 199-bp random dsDNA chains in a 250 mM salt concentration, $N_{DNA} = 1.1 \pm 0.9$ (n = 3) (orange bars in Fig. 2d, Supplementary Fig. 5a(iii), and Supplementary Movie 5). While the effective concentration and stoichiometry used in MD simulations is different from what is employed in the experimental measurements in order to improve

sampling efficiency, the dramatic decrease of the protein-DNA bridging capacity due to the TAD addition (MD 2) and the salt concentration increasement (MD 3) is consistent with the above experimental observations, highlighting the critical role of p53 bridging across different DNA duplexes for DPIC formation.

From the above MD simulations, we also determined the average dwelling time for a p53 core DBD binding with one DNA duplex, which was named as "Lifetime of p53 core DBD binding with one DNA duplex" (Supplementary Fig. 4a and **Supplementary Methods**). The average Lifetime in MD 1 (150 mM NaCl) is $(1.20 \pm 0.06) \times 10^6$ (n = 3) MD steps (Fig. 2e). Upon salt concentration increases to 250 mM, the value dramatically decreased to $(0.59 \pm 0.05) \times 10^6$ (n = 3) MD steps (MD 3 in Fig. 2e), demonstrating the salt-resulted weakening of p53-dsDNA bridging interactions.

In this context, we introduce the term "ε_{app}" to denote the apparent inter-molecule interaction strengths within the DPIC. Given the distinctive microscopic structure of DPIC, the number of bridges, symbolized by p53 molecules on each DNA, and the binding affinity between DNA and protein serve as two important factors governing ε_{app}.

Increasing the ε_{app} induces a morphological transition from a droplet-like to a "pearl chain"-like structure

We observed that changing the initial molar ratio between p53 and DNA has the potential to modify the number of bridges formed on each DNA. Similarly, modifications in the DNA sequence can impact the binding affinity between DNA and protein. Consequently, varying the initial molar ratio between p53 and DNA, as well as manipulating the DNA sequence, emerge as two experimental approaches for fine-tuning the ε_{app}. Our

subsequent inquiry aimed to elucidate the regulatory role of ε_{app} in governing DPIC formation.

First is changing the initial molar ratio between p53 and DNA. The phase diagram presented in Fig. 1c reveals that: (*i*) at 20 μM p53^{4M} ΔTAD, 0.9 μM 400-bp random DNA substrates exhibit detectable droplet-like DPIC formation, whereas concentrations below 0.3 μM of DNA initiate a formation of distinguishable "pearl chain"-like DPICs; (*ii*) at 0.15 μM 400-bp random DNA substrates, 5 μM p53^{4M} ΔTAD shows detectable droplet-like DPIC formation, whereas concentrations exceeding 10 μM protein also initiate the formation of distinguishable "pearl chain"-like DPICs. These results suggest that altering the initial molar ratio between p53 and DNA (m = [p53] / [DNA]) can influence DPIC morphology.

To examine this aspect carefully, we conducted two-color *in vitro* droplet assays by combining 20 μM p53^{4M} ΔTAD labeled with ATTO565 and varying concentrations of 400-bp random DNA labeled with FAM (0, 0.075, 0.15, 0.225, 0.3, 0.375, 0.45, 0.6, 0.75, 0.9, 1.2, 1.5, and 1.8 μM) (Fig. 3a). Notably, at 1.8 μM 400-bp random DNA, droplet-like DPICs were readily observable, corresponding to an m value of 20/1.8 = 11.1. However, as the DNA concentration decreased to 0.225 μM, a transition in DPIC morphology from droplet-like to "pearl chain"-like occurred, coinciding with an increase in m from 11.1 to 88.9. These outcomes strongly imply that an increase in m results in a higher number of bridges on each DNA, thereby transitioning the DPIC morphology from droplet-like to "pearl chain"-like. Furthermore, there exists a threshold for m (m_{th}), approximately m_{th} = 66.7, beyond which "pearl chain"-like DPIC formation is induced.

To assess the actual molar ratio within the DPIC, we measured the fluorescent intensity ratio of p53^{4M} ΔTAD (ATTO565) / DNA (FAM). Our findings revealed that the n value for droplet-like DPICs is substantially lower than that of "pearl chain"-like DPICs (Fig. 3b), confirming that the number of bridges on each DNA, which is an important factor governing ε_{app}, can regulate the morphology transition of DPICs.

Second is changing the DNA sequence. EMSAs revealed a significantly enhanced binding affinity of p53^{4M} ΔTAD to the p21 binding motifs compared to random DNA (Supplementary Fig. 2b). Subsequently, we explored whether the addition of p21 binding motifs into the DNA sequence, thereby strengthening ε_{app}, could also modulate the morphology of DPICs.

We devised new *in vitro* droplet assays. In contrast to the droplet-like morphology observed with 400-bp random DNA in conjunction with p53^{4M} ΔTAD (Fig. 1b(i) and Supplementary Movie 1), the combination of 0.6 μM 400-bp DNA containing 3× p21 binding motifs with 20 μM p53^{4M} ΔTAD also facilitated the formation of "pearl chain"-like DPICs (Fig. 4a and Supplementary Movie 6). A comprehensive examination of these "pearl chain"-like co-condensates was undertaken through: (*i*) *in vitro* droplet assays involving the mixing of 0, 0.15, 0.3, 0.6, and 0.9 μM 400-bp DNA containing 3× p21 binding motifs with 10, 20, and 40 μM dark p53^{4M} ΔTAD (Fig. 4b); (*ii*) *in vitro* droplet assays incorporating the mixing of 0.6 μM 400-bp DNA containing varying numbers of p21 binding motifs (0×, 1×, 2×, 3×, and 4×) with 0, 10, 20, and 40 μM dark p53^{4M} ΔTAD (Fig. 4c). The results demonstrated a "pearl chain"-like morphology in DPICs when the DNA substrate carried multiple copies of the p21 sequence. To observe the morphological transition, we mixed 400-bp DNA containing 3× p21 binding motifs with 400-bp random DNA, generating

0.6 μM 400-bp DNA substrates with varying concentrations of p21 sequences (Fig. 4d). At 20 μM p53^{4M} ΔTAD, 0.6 μM DNA substrates devoid of p21 exhibited detectable droplet-like DPIC formation. Beyond a concentration of 0.3 μM for 400-bp DNA containing 3× p21 binding motifs, these DNA substrates initiated the formation of discernible "pearl chain"-like DPICs. These findings confirm that increasing the binding affinity between dsDNA and protein can also induce a morphological shift from droplet-like to "pearl chain"-like.

Analogous to the droplet-like DPICs induced by random DNA, the "pearl chain"-like DPIC is profoundly responsive to NaCl concentration but remains unaffected by the presence of 1,6-HD (Fig. 4e-f). This outcome underscores that the formation of "pearl chain"-like DPICs is also predominantly driven by electrostatic interactions rather than hydrophobic interactions.

In addition to the incorporation of p21 binding motifs, manipulating salt concentration, which can regulate the binding affinity between DNA and protein, can also alter the ε_{app}. Notably, a reduction in salt concentration from 250 mM to 120 mM induced a morphological transition in DPICs formed by 0.15 μM 400-bp random DNA mixed with 20 μM p53^{4M} ΔTAD, shifting from a droplet-like to a "pearl chain"-like configuration (Supplementary Fig. 2d). In conclusion (Fig. 3-4), our results emphasize that increasing the ε_{app} induces a morphological transition from a droplet-like to a "pearl chain"-like structure

Increasing the ε_{app} induces phase transition of droplet-like DPICs

Recent literature extensively discusses the viscoelastic nature of nucleic acid and protein co-condensation, both *in vitro* (Alshareedah *et al.*, 2021; Alshareedah *et al.*, 2022) and *in*

vivo (Strom et al., 2023). Our fusion experiments and FRAP experiments (Fig. 1d-f) consistently point towards distinctive material characteristics of DPICs. Leveraging the AFM-FS technique, which has proven effective in probing the mechanical properties of biomolecular condensates, we next asked whether we can conduct measurements to unveil the material properties of DPIC (**Methods** and Fig. 5a(i)).

To quantitatively assess viscoelasticity, we conducted an AFM-FS experiment known as the stress relaxation test (Fig. 5a(ii)) (Chaudhuri et al., 2020). In these experiments, the AFM probe descended to a specific height (~0.3 μm in Fig. 5b(i)) for 1 second, capturing a relaxation curve of force over this period (Fig. 5b(ii)). We employed a generalized Maxwell model featuring one spring and two Maxwell elements in parallel to fit these normalized relaxation curves (**Supplementary Methods**, Fig. 5b(iii), and Supplementary Fig. 6) (Moreno-Flores et al., 2010b; Weber et al., 2019). The spring contributes a pure elastic effect, evident in the A_0 term. The two Maxwell elements represent two relaxation stages, where A_1 and A_2 correspond to the force decay of the elements, and τ_1 and τ_2 represent the relaxation time. The relaxation time correlates with the viscosity of the DPIC. Specifically, $A_0 = 1 – A_1 – A_2$. When $A_0 = 0$, the DPIC behaves as a viscoelastic fluid. Conversely, when $A_0 > 0$, the DPIC exhibits viscoelastic solid characteristics (Chaudhuri *et al.*, 2020). Due to methodological constraints, AFM-FS experiments could only be conducted on samples exhibiting a droplet-like DPIC morphology (Fig. 5c).

We initiated the stress relaxation test for droplet-like DPICs composed of 0.6 μM 400-bp random DNA mixed with 20 μM $p53^{4M}$ ΔTAD (Fig. 5c(i)), and the stress relaxation curve was subsequently normalized (the blue curve in Fig. 5c(iv)). The values obtained are as

follows: A_0 of 0.04 ± 0.03 (mean ± s.d., N = 20), τ_1 of 0.26 ± 0.03 seconds (mean ± s.d., N = 20), and τ_2 of 0.022 ± 0.003 seconds (mean ± s.d., N = 20). Given that A_0 is close to zero, this outcome implies that this particular DPIC exhibits viscoelastic fluid-like behavior.

Using this condition as a reference, we conducted two additional AFM-FS experiments: (*i*) examining droplet-like DPICs comprising 0.3 μM 400-bp random DNA mixed with 20 μM $p53^{4M}$ ΔTAD (Fig. 5c(ii)), with the generalized Maxwell model (Fig. 5b(iii)) applied to fit the curve (orange curve in Fig. 5c(iv)): A_0 of 0.13 ± 0.03 (mean ± s.d., N = 23), τ_1 of 0.28 ± 0.08 seconds (mean ± s.d., N = 23), and τ_2 of 0.028 ± 0.005 seconds (mean ± s.d., N = 23); (*ii*) investigating droplet-like DPICs composed of 0.6 μM 400-bp DNA (90% random DNA and 10% DNA containing 3× p21 binding motifs) mixed with 20 μM $p53^{4M}$ ΔTAD (Fig. 5c(iii)), with the generalized Maxwell model (Fig. 5b(iii)) employed to fit the curve (green curve in Fig. 5c(iv)): A_0 of 0.19 ± 0.02 (mean ± s.d., N = 25), τ_1 of 0.33 ± 0.04 seconds (mean ± s.d., N = 25), and τ_2 of 0.030 ± 0.004 seconds (mean ± s.d., N = 25). These findings indicate that A_0 is greater than zero in both conditions (Fig. 5c(v)), corresponding a viscoelastic solid regime. Therefore, the above results suggest a phase transition from viscoelastic fluid to viscoelastic solid for droplet-like DPICs when increasing the number of bridges on each DNA or the binding affinity between DNA and protein.

Two types of transitions in the two-component phase diagram of DPICs combining $p53^{4M}$ ΔTAD and 400-bp random DNA

To characterize the molecular mechanism of DPICs, we aimed to construct a two-component phase diagram. We conducted three sets of two-color *in vitro* droplet assays

by (*i*) combining 20 μM p53^{4M} ΔTAD labeled with ATTO565 and varying concentrations of 400-bp random DNA labeled with FAM (ranging from 0, 0.075, 0.15, 0.225, 0.3, 0.375, 0.45, 0.6, 0.75, 0.9, 1.2, 1.5, to 1.8 μM) (Fig. 3a); (*ii*) combining 5 μM p53^{4M} ΔTAD labeled with ATTO565 and varying concentrations of 400-bp random DNA labeled with FAM (ranging from 0, 0.075, 0.15, 0.225, 0.3, 0.45, 0.6, to 0.9 μM) (Fig. 6a); (*iii*) combining 0.075 μM 400-bp random DNA labeled with FAM and varying concentrations of p53^{4M} ΔTAD labeled with ATTO565 (ranging from 0, 2.5, 5, to 10 μM) (Fig. 6b). By measuring the intensity of p53^{4M} ΔTAD (ATTO565) and 400-bp random DNA (FAM) in both the dense and dilute phases, we generated a two-component phase diagram of DPIC (Fig. 6c). The coexistence region is centrally located, encompassing all tie lines that connect both the dense and dilute phases for each condition. Interestingly, all tie lines exhibit positive slopes, indicative of cooperativity between the components.

The slopes of these tie lines exhibit interesting variation (Supplementary Fig. 7a-c), delineating two distinct thresholds indicative of different transitions. Our AFM-FS experiments revealed that despite both types of DPICs, one composed of 0.6 μM 400-bp random DNA mixed with 20 μM p53^{4M} ΔTAD (Fig. 5c(i)) and the other of 0.3 μM 400-bp random DNA mixed with 20 μM p53^{4M} ΔTAD (Fig. 5c(ii)), exhibiting a droplet-like morphology, the former, with 0.6 μM DNA, displays characteristics of a viscoelastic fluid, while the latter, with 0.3 μM DNA, exhibits properties of a viscoelastic solid. Thus, the first slope threshold, around 2.2, which is the slope of DPIC formed by 0.6 μM 400-bp random DNA mixed with 20 μM p53^{4M} ΔTAD (orange line in Supplementary Fig. 7d), signifies a phase transition between viscoelastic fluid and viscoelastic solid. The second slope threshold, which is located at the DPIC consisting of 0.225 μM 400-bp random DNA mixed

with 20 μM $p53^{4M}$ ΔTAD, approximately 0.9 (blue line in Supplementary Fig. 7d and Fig. 3a), indicates a morphology transition between DPICs with droplet-like morphology and those with "pearl chain"-like morphology. The transition in morphology prompted us to further investigate the molecular mechanisms underlying DPICs in the following two sections.

Droplet-like and "pearl chain"-like DPICs can give rise to comparable nanometer-sized CMCs near the saturation concentration condition

In previous experiments, we found that DPIC is mainly formed by fusion (Fig. 1b and e). So, we define the basic unit of DPIC fusion as critical microscopic cluster (CMC). In this section, we want to explore whether we could quantitatively measure and compare the size of the CMCs for both droplet-like and "pearl-chain"-like DPICs. Drawing from the theory of phase separation (Alberti et al., 2019), we posited an assumption: when the initial concentrations of protein and DNA decrease to saturation concentration (C_{sat}), the total volume fraction of DPICs becomes exceedingly small, and the size of a single DPIC corresponds to a CMC.

The spatial constraints imposed by the optical diffraction limit (~200 nm) in confocal fluorescence microscopy for *in vitro* droplet assays present a challenge in measuring nanometer-sized CMCs (Supplementary Fig. 2e). To accurately quantify the CMCs, we employed a confocal-based fluorescence fluctuation microscopy – the dual-color fluorescence cross-correlation spectroscopy (dcFCCS) assay (Fig. 7a) (Peng et al., 2020; Yao et al., 2022). We labeled $p53^{4M}$ ΔTAD and 400-bp DNAs with Cyanine5 (Cy5) and FAM, respectively (Fig. 7a(i)). These labeled components freely diffused through the

confocal detecting volume (Fig. 7a(ii)). Upon protein-DNA heterocomplex formation, the signals from protein and DNA contributed to the cross-correlation curves, and the relaxation times of these curves facilitated the precise quantification of the hydrodynamic radii of DPICs (Fig. 7a(iii)).

Maintaining a fixed ratio of $p53^{4M}$ ΔTAD to 400-bp DNA concentrations at 20:0.6, we conducted a series of experiments with increasing concentration (Fig. 7b(i)). For random DNA, known to induce droplet-like DPICs (Fig. 1b), when the concentrations of $p53^{4M}$ ΔTAD and DNA were below 1 μM and 0.03 μM, respectively, the participation ratios of $p53^{4M}$ ΔTAD and DNA were notably low (Fig. 7b(ii)-(iii)). This suggests that most proteins and DNAs did not partake in protein-DNA heterocomplex formation. However, with concentrations of $p53^{4M}$ ΔTAD and DNA at 1 μM and 0.03 μM or higher, respectively, both the participation ratios and hydrodynamic radii of heterocomplex showed a significant increase (Fig. 7b(ii)-(iii) and d(i)). The sharp rise in the participation ratio at 1 μM $p53^{4M}$ ΔTAD and 0.03 μM 400-bp random DNA indicates this as the C_{sat} condition for droplet-like DPICs.

Similarly, for DNA containing 3× p21 binding motifs, capable of inducing “pearl chain”-like DPICs (Fig. 4a), increasing protein and DNA concentrations resulted in elevated participation ratios and hydrodynamic radii of protein-DNA heterocomplex (Fig. 7c and d(ii)). The participation ratios of proteins and DNAs significantly increased at 0.75 μM $p53^{4M}$ ΔTAD and 0.023 μM 400-bp DNA containing 3× p21 binding motifs, marking this as the C_{sat} condition for “pearl chain”-like DPIC. At their respective C_{sat} conditions, there was no significant difference in the hydrodynamic radius between droplet-like DPICs and “pearl chain”-like DPICs (Fig. 7d(iii)). This result suggests that both droplet-like DPICs

and “pearl chain”-like DPICs encompass a stage of CMCs with a consistent size of about 15-30 nm. Additionally, the noted CMC size of DPICs containing cGAS and dsDNA is approximately 70 nm (Yao *et al.*, 2022), indicating potential variability in CMC sizes across different types of DPICs. Remarkably, beyond the C_{sat} conditions, even slight increases in the concentration of protein and DNA, such as 0.06 μM 400-bp DNA and 2 μM $p53^{4M}$ ΔTAD, resulted in 4-time differences in hydrodynamic radius between droplet-like DPICs and “pearl chain”-like DPICs (Fig. 7d(iv)). This phenomenon was not observed with the confocal microscopy, which suggested the calculation of the hydrodynamic radius was affected by morphological change (Supplementary Fig. 2e).

Increasing the ε_{app} leads to a prolonged relaxation time, thereby governing the morphology of DPICs

As the sizes of droplet-like CMC and “pearl chain”-like CMC are same, we next asked whether the different ε_{app} can affect the condensate coalescence, regulating the DPIC morphology. We constructed a two-dimensional off-lattice model (**Supplementary Methods**), in which $p53^{4M}$ ΔTAD was simplified to a star-shaped structure with four branching beads connecting to a central bead, and DNA was simplified to a straight but flexible chain consisting of 7 beads (Fig. 8a(i)). The branching beads of $p53^{4M}$ ΔTAD tetramer interact with the DNA beads through the Lennard-Jones potential with the strength controlled by a parameter λ (Fig. 8a(ii)). The simulation system contains 2,400 $p53^{4M}$ ΔTAD tetramers and 1,400 DNA chains, which were randomly placed in a squared box of ~333 $\sigma \times 333\ \sigma$, with σ being the reduced length unit. We performed Langevin dynamics simulations at the temperature of 298 K. When the λ values are larger than 10,

the molecules in the system formed large condensates, which allows us to investigate the relation between the ε_{app} and the physical properties of the formed condensates.

As shown by the final structures of the simulations, the condensates were nearly round-shaped when λ was low, suggesting liquid-droplet like property (Fig. 8b(i) and Supplementary Movie 7). In comparison, the condensates became "pearl chain"-like when λ was higher (Fig. 8b(ii) and Supplementary Movie 8). More quantitative characterization showed that increasing interaction strength λ tends to decrease the circularity of condensates (Fig. 8b(iii)). Such results were highly consistent with the above experimental observation that increased protein-DNA interaction strengths tend to drive the formation of condensates with "pearl chain"-like morphology. We also characterized the dynamic property of the condensate by calculating the diffusion coefficient (D) of the protein molecules within the condensates (Supplementary Fig. 8). As expected, the diffusion coefficient decreases monotonically with the increasing of protein-DNA interaction strengths, demonstrating arrested molecular mobility with stronger protein-DNA interactions. We further calculated the diffusion time ($\tau_D = L^2/4D$, with L being the radius of the observed droplet) to roughly characterize the relaxation time (τ) of protein-DNA scaffold inside the DPICs (Fig. 8c(i)), which showed an anticorrelation with circularity (Fig. 8c(ii)).

To assess the exclusive impact of relaxation time on condensate morphology, we constructed a mathematical model based on viscoelastic phase separation (VPS) theory proposed by Hajime Tanaka (Fig. 8d and **Supplementary Methods**) (Tanaka, 2000). We optimized parameters such as the interaction parameter (χ), modulus of bulk stress (G_B), modulus of shear stress (G_S), and others, to fit the DPIC system (Jawerth et al., 2020). In

the initial state, droplets of uniform size, which mimicked CMCs in the previous session, were randomly situated in a square box with periodic boundary conditions (Fig. 8d(i), (iii), (v), and (vii)). While maintaining all other parameters constant, we exclusively altered the maximum values of relaxation times (τ_{max}) for bulk and shear stress, acting as regulators of the droplets' mechanical properties. The systems evolved over 5,000 steps as per Eq. (1)-(3) in Supplementary Methods. The dynamics and final morphology of the condensates displayed substantial variability with τ_{max}. A small τ_{max} (e.g., 0 or 1) led to rapid fusion, resulting in large, round droplets (Fig. 8d(ii), (iv), and Supplementary Movie 9-10). Conversely, a larger τ_{max} (e.g., 100) allowed for droplet fusion but maintained slower deformation, resulting in aspheric morphology (Fig. 8d(vi) and Supplementary Movie 11). Extremely high τ_{max} (e.g., 10,000) led to the coalescence of initial droplets but hindered complete integration, preserving a "pearl chain"-like morphology (Fig. 8d(viii) and Supplementary Movie 12). As τ_{max} was the only variable in this model, these outcomes underscored that altering relaxation time alone could be enough to induce morphological changes.

These results may suggest a plausible interpretation for the observed morphology change in the above experimental measurements. When the ε_{app} is relatively weak, the p53 bridged DNA network formed in the condensates can rearrange rapidly, which leads to fast relaxation of the condensates to the energetically favorable round shape, demonstrating the droplet-like morphology. However, when the ε_{app} is strong, the rearrangement of the molecular network in the condensates becomes slow and the timescale needed for the shape relaxation can be much longer than the measurement timescale, which leads to the "pearl chain"-like morphology.

This enlightens us on whether it is possible to record the rounding of "pearl chain"-like DPIC by extending the observation time. The results showed that DPIC formed by 20 μM $p53^{4M}$ ΔTAD and 0.6 μM 400-bp DNA containing 3× p21 binding motifs was “pearl chain”-like when the incubation time was only 30 minutes. Interestingly, when the incubation time was extended to 16 hours, the morphology of this sample changed greatly, with the circularity increased significantly (Supplementary Fig. 9). This indicates that “pearl chain”-like DPIC with higher ε_{app} does have a longer relaxation time, and it must be accompanied by a longer observation time to see the relaxation process.

Discussion

In this work, we utilized p53 as a model system to elucidate the biophysical mechanisms underlying DPIC (Fig. 9), representing a simplified instance of the co-condensation of two-component nucleic acid and protein. These co-condensation processes are crucial for unraveling the physical chemistry involved in more intricate multi-component phase separations within living cells, thereby making substantial contributions to diverse biological functions.

Our research demonstrated that $p53^{4M}$ ΔTAD has the capacity to form DPIC with dsDNA, wherein the microscopic structure involves the bridging of different DNA duplexes by $p53^{4M}$ ΔTAD (Fig. 9b(i)). Interestingly, these microscopic structures are consistent with those found in cohesion complexes with DNA (Ryu et al., 2021), KLF4 complexes with DNA (Sharma *et al.*, 2021), as well as human cGAS complexes with DNA (Xie et al., 2019). We observed that the DPIC morphology can transition from droplet-like to a “pearl chain”-like structure by increasing the number of bridges on each DNA or the binding

affinity between DNA and protein (Fig. 3-4 and 9b(ii)). *In vitro* droplet assays were conducted to construct the two-component phase diagram of DPICs (Fig. 3 and 6), revealing two transitions (Fig. 9a(i)). The first is a phase transition between viscoelastic fluid and viscoelastic solid, as supported by experimental findings from AFM-FS (Fig. 5). The second is a morphology transition between droplet-like DPIC and "pearl chain"-like DPIC.

Based on established principles in soft matter physics concerning nucleation, growth, and coarsening (Berry *et al.*, 2018; Tanaka, 2022), we subsequently introduced a model to elucidate DPIC behavior, which was validated through dcFCCS (Fig. 7), accompanied by the establishment of two mathematical models (Fig. 8). Our model (Fig. 9b(i)) delineates two distinct stages in the DPIC formation process. In the initial stage (Stage I), initial nucleation and diffusion-limited growth driven by protein-DNA interaction lead to the formation of CMCs with a radius of approximately 15-30 nm (Fig. 7). The crosslinking and/or entanglement between the DNA and protein makes CMC to behave viscoelastic properties. While we cannot directly measure the viscoelastic properties of CMCs, it is reasonable to infer that these CMCs have the same viscoelasticity as DPICs, which is verified by AFM-FS (Fig. 5).

In the subsequent stage (Stage II), these CMCs coalesce into larger droplets through processes such as diffusion-limited coarsening (DLC or Ostwald ripening) or Brownian motion coalescence (BMC). We introduce the term "ε_{app}" to denote the apparent inter-molecule interaction strengths. Increasing either the number of bridges on each DNA or the binding affinity between DNA and protein (Fig. 9b(ii)) serves to enhance the intermolecular interaction strengths (ε_{app}), consequently leading to an increasement in the

relaxation time within these CMCs and between these CMCs. This heightened interaction strength induces a morphological transition from a droplet-like to a “pearl chain”-like structure, as depicted in Fig. 8.

Based on our data, several interesting topics warrant further discussion in future studies. First is about the two-component phase diagram of DPICs (Fig. 9a(i)). Dignon and colleagues comprehensively reviewed four distinct types of phase diagrams for a two-component system (Dignon et al., 2020): cooperative, scaffold-client, cross-interaction-driven, and exclusive cophase separation. Within the framework of cross-interaction-driven cophase separation, each species is incapable of undergoing phase separation independently, and only the mutual attraction between both species induces cophase separation. As discussed earlier, neither $p53^{4M}$ ΔTAD nor dsDNA can undergo LLPS independently (Fig. 1c and Supplementary Fig. 1e), suggesting that the protein-protein interactions (ε_{AA}) and the dsDNA-dsDNA interactions (ε_{BB}) are weak, with protein-dsDNA interactions (ε_{AB}) predominantly governing the overall DPIC system. Consequently, the phase paradigm characterizing our DPIC system, formed by the combination of $p53^{4M}$ ΔTAD and 400-bp random DNA, represents a unique instance of the cross-interaction-driven cophase separation paradigm (Fig. 9a(i)-(ii)). Interestingly, in comparison to the cross-interaction-driven cophase separation model ($\varepsilon_{AA} = \varepsilon_{BB} \sim 0$, and $\varepsilon_{AB} > 0$) proposed by Dignon and colleagues (Dignon *et al.*, 2020), our phase diagram (Fig. 6c and Supplementary Fig. 7) reveals dynamic changes in all positively sloped tie lines within the coexistence region (Fig. 9b(i)). We assumed that although $p53^{4M}$ ΔTAD molecules are unable to undergo LLPS, there still exist inter-molecular interaction

strengths between p53^{4M} ΔTAD molecules, indicating $\varepsilon_{AA} > 0$ (Fig. 9b(ii)). This condition ($\varepsilon_{AA} > 0$ but no LLPS, $\varepsilon_{BB} \sim 0$, and $\varepsilon_{AB} > 0$) poses an interesting topic for future study.

We also notice that our cross-interaction-driven cophase separation paradigm delineates two distinct transition behaviors (Fig. 9a(i)). As the slope of tie lines progressively diminishes, the initial transition signifies a phase shift between viscoelastic fluid and viscoelastic solid. It is crucial to emphasize that the droplet-like morphology of DPICs persists during this phase transition. The second type of transition becomes evident as the slope of the tie lines continues to decrease, indicating a morphology transition from DPICs with droplet-like characteristics to those exhibiting a "pearl chain"-like morphology. These findings underscore that the phase transition from viscoelastic fluid to viscoelastic solid does not instantaneously alter the morphology of DPICs; rather, the transition in morphology is distinctly driven by the presence of more viscoelastic solids. We speculate that the molecular mechanism governing both transitions involves the modulation of two critical relaxation times by tuning ε_{app}, thus opening up another interesting topic for future exploration.

Material properties of single-component condensates has been extensively studied both *in vitro* (Molliex *et al.*, 2015; Patel et al., 2015) and *in vivo* (Dorone et al., 2021; Shin et al., 2017). These condensates have been established as not being simple liquids (Jawerth *et al.*, 2020), and the interaction strengths between the single-component macromolecules are the key parameters driving the phase transition from a liquid-like state to a gel-like or solid-like condensed states (Shin and Brangwynne, 2017). In contrast to single-component condensates, the molecular mechanisms dictating the physical properties of multi-component condensates remain elusive. Interestingly, biomolecular

condensates containing dsDNA, such as nucleosomal arrays, exhibit diverse material properties, ranging from liquid-like (Gibson *et al.*, 2019; Larson *et al.*, 2017; Wang *et al.*, 2019) to gel/solid-like (Hansen *et al.*, 2021; Strickfaden *et al.*, 2020). We also speculate that altering the material properties of DPICs, transitioning between a viscoelastic fluid and a viscoelastic solid while maintaining the droplet-like morphology, could serve as a valuable strategy for living cells to finely regulate essential cellular processes. This includes processes like transcription and repair within various biomolecular condensates that involve nucleic acids. This is also another interesting topic for the future study.

Second, in delineating the coarsening mechanism during Stage II of DPIC formation (Fig. 9b(i)), distinguishing between Ostwald ripening (Lifshitz and Slyozov, 1961; Zhang et al., 2021) and BMC proves elusive. However, recent investigations by Brangwynne and colleagues have underscored a proclivity for biomolecular condensates to undergo coarsening primarily through BMC (Lee et al., 2021). Our two-color experiments in Fig. 1e can also support the BMC may be the dominant mechanism during the Stage II. The fourth promising avenue for future exploration involves a comparative analysis of the similarities between biomolecular condensates within a living cell and VPS in the realm of soft matter physics (Tanaka, 2022).

Third, this conceptual framework of our model in Fig. 9 finds relevance in the context of a recent discourse on phase separation coupled to percolation (PSCP) (Mittag and Pappu, 2022). Through MD simulations (Fig. 2), we observed that DPICs exhibited an organized network structure attributed to the bridging effect of p53 between different DNA chains. Additionally, given the viscoelastic physical properties exhibited by DPICs (Fig.

5), we postulate that the formation of DPICs may entail a percolation process. This intriguing aspect warrants another further exploration in future studies.

In summary, our findings offer a quantitative characterization of the phase-separation mechanism of DPIC. Moreover, they present a novel avenue for comprehending the intricate world of multi-component condensates within living cells. Ultimately, these insights may pave the way for the manipulation of biomolecular condensation behaviors, offering innovative strategies for intervening in human diseases.

Acknowledgments

We thank the Peking Nanofab for process support. We thank the National Center for Protein Sciences at Peking University in Beijing, China, particularly Dr. Siying Qin, for technical help with AFM. We thank the computational support from the High-Performance Computing Center of Nanjing University. We thank Dr. Luhua Lai (Peking University), Dr. Sheng Mao (Peking University), Dr. Ming Han (Peking University), Dr. Chun Tang (Peking University), and members of the Qi laboratories for comments on the manuscript.

Author Contributions

C.L. prepared biological samples, conducted all experiments, performed data analysis, and wrote the manuscript. Y.B. and W.L. conducted the coarse-grained molecular dynamics and two-dimensional off-lattice model. Y.T. and C.C. conducted the dcFCCS experiments and performed data analysis. L.M. and J.L. conducted numerical simulations

of viscoelastic phase separation. P.Y. developed *in vitro* p53 purification protocol and *in vitro* droplet assay for p53 condensate study. Y.H. and J.C. assisted C.L. Y.L. helped to purify $p53^{4M}$ ΔTAD. Z.Q., W.L., and C.T. supervised the project, experimental designs, and data analysis. Z.Q. and W.L. wrote the manuscript with input from all authors.

Funding

This work was supported by National Natural Science Foundation of China (Grant No. T2225009 (Z.Q.), T2321001, 31670762 (Z.Q.), 32088101, and 11974173 (W.L.), 21922704, 22061160466, and 22277063 (C.C.)). The grant of Wenzhou Institute, University of Chinese Academy of Sciences (WIUCASQD2022034 (Y.B.) and WIUCASQD2021010) (W.L.)).

Figures

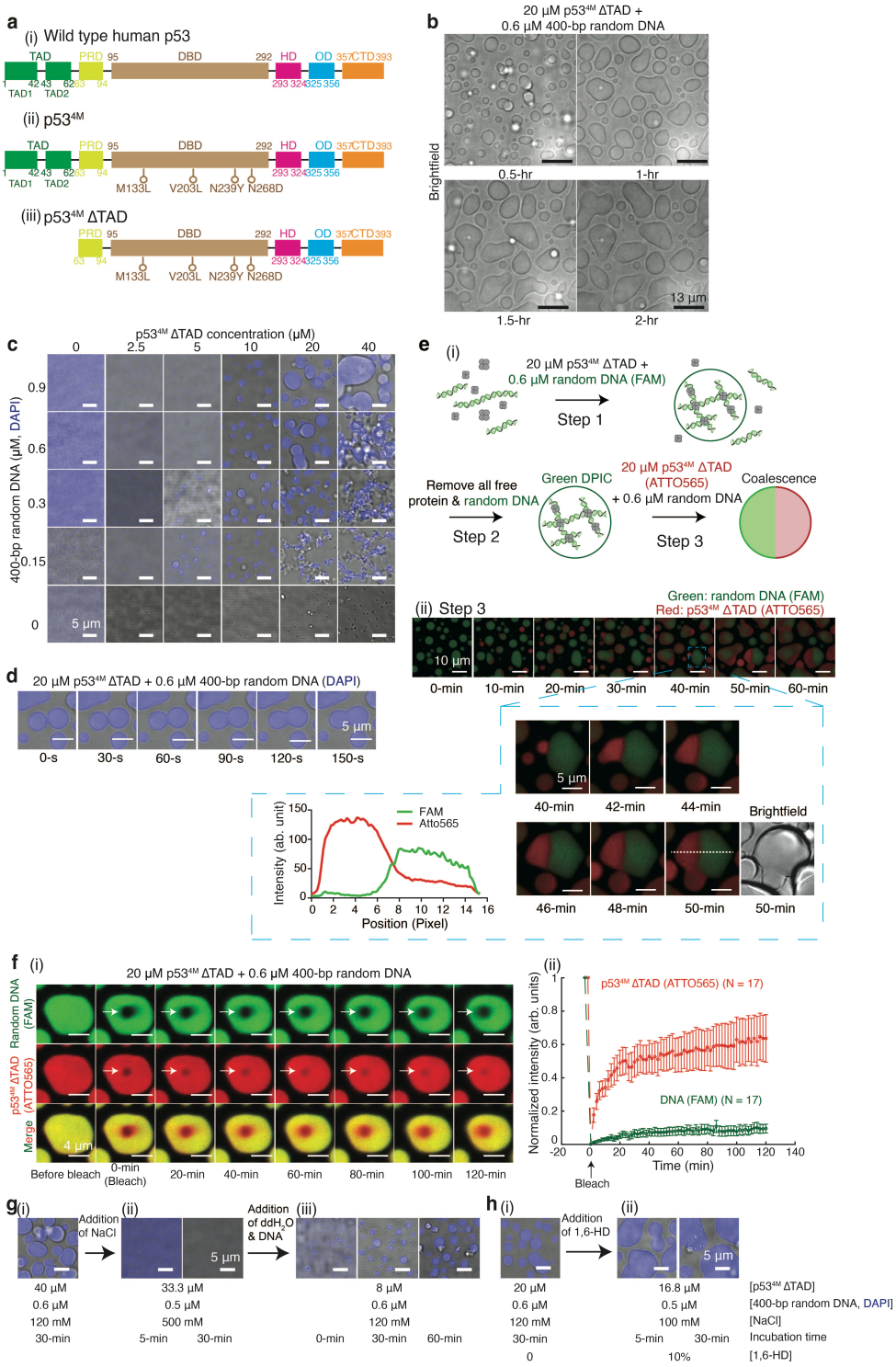

Fig. 1. Formation of droplet-like DPICs by p53^{4M} ΔTAD with random dsDNA. (**a**) Schematic representation of WT human p53 (i), p53^{4M} (ii), and p53^{4M} ΔTAD (iii). (**b**) Time

course of the fusion event between 20 μM p53^{4M} ΔTAD and 0.6 μM 400-bp random DNA (Supplementary Movie 1), with time indicated in hours. (**c**) *In vitro* droplet assays mixing 0, 0.15, 0.3, 0.6, and 0.9 μM 400-bp random DNA with 0, 2.5, 5, 10, 20, and 40 μM dark p53^{4M} ΔTAD, where DNA was labeled with DAPI. (**d**) Time course of the fusion event between two droplet-like DPICs from (b), with time indicated in seconds. (**e**) Two-color experiment. (i) Schematic of the process: Step 1, formation of green DPICs by mixing 20 μM dark p53^{4M} ΔTAD and 0.6 μM 400-bp random DNA labeled with FAM; Step 2, removal of free protein and DNA by washing; Step 3, injection of a new sample containing 20 μM p53^{4M} ΔTAD labeled with ATTO565 and 0.6 μM dark 400-bp random DNA. (ii) Time course of coalescence of two color-labeled DPICs, with time indicated in minutes. The box zooms in on a representative fusion event between 40 and 50 min, and fluorescence intensities at 50 min are plotted. (**f**) FRAP assay. (i) DPICs formed by 0.6 μM 400-bp random DNA labeled with FAM and 20 μM p53^{4M} ΔTAD labeled with ATTO565, with a 2-hour incubation and 2-hour recovery process recorded. (ii) FRAP curves with red indicating p53^{4M} ΔTAD (ATTO565) and green indicating DNA (FAM). Seventeen independent DPICs were plotted (N = 17). Error bars represent mean ± s.d. (**g**) (i) Formation of a droplet-like DPIC with 40 μM p53^{4M} ΔTAD and 0.6 μM 400-bp random DNA under 120 mM NaCl; (ii) Addition of NaCl to 500 mM and incubation for 5 min or 30 min at room temperature; (iii) Addition of water and DNA to decrease the salt concentration back to 120 mM NaCl and incubation for 5 min or 30 min at RT. (**h**) (i) Formation of a droplet-like DPIC with 20 μM p53^{4M} ΔTAD and 0.6 μM 400-bp random DNA under 0% 1,6-hexanediol (1,6-HD); (ii) Addition of 1,6-HD to 10% and incubation for 5 min or 30 min at room temperature. The working buffer for in vitro droplet experiments

was 8 mM Tris-HCl (pH 7.5), 120 mM NaCl, 4% Glycerol, and 16 mM DTT. The working buffer contained no crowding agents in this study. Independent *in vitro* droplet experiments in b to h were repeated three times (n = 3) respectively.

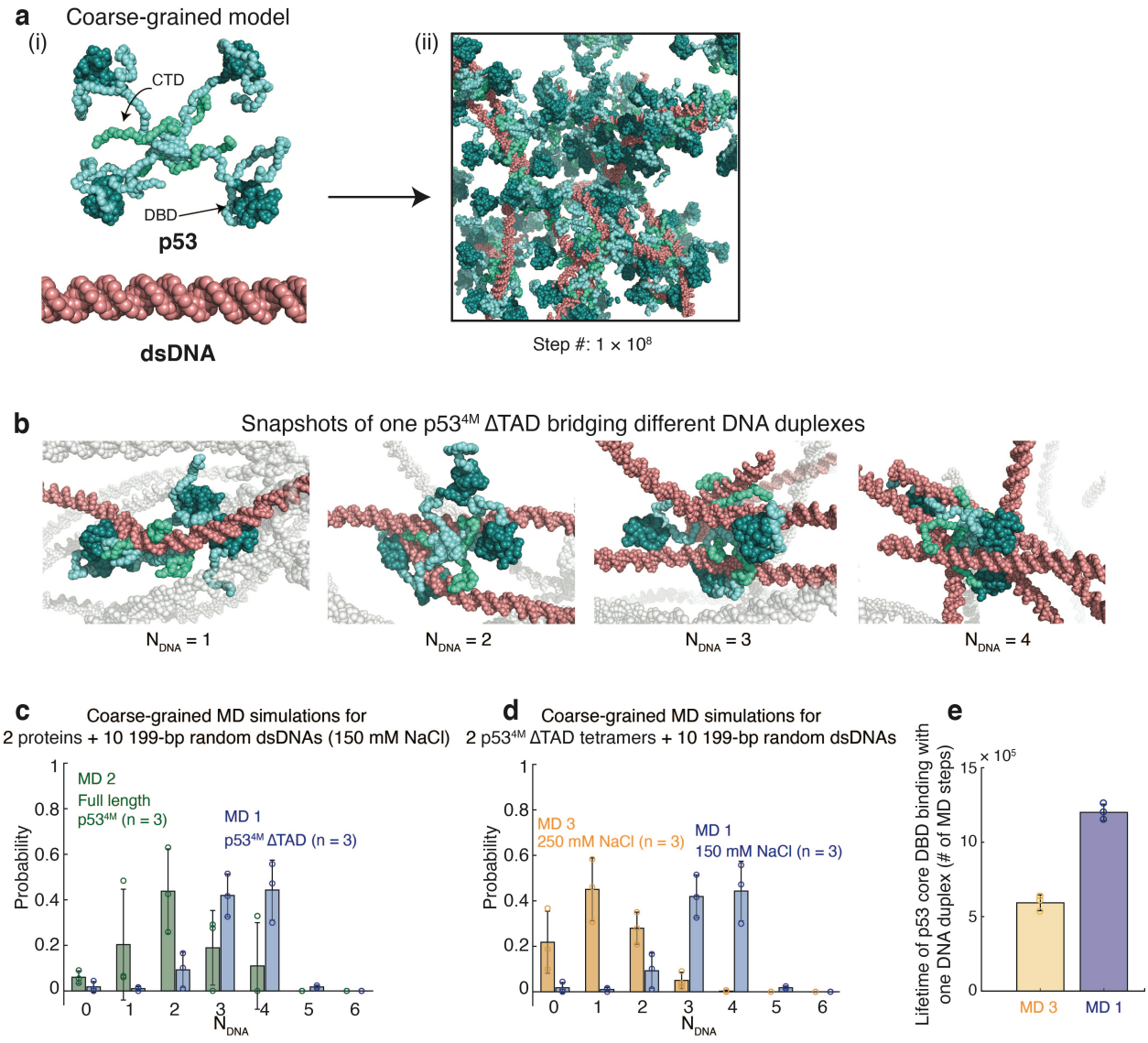

Fig. 2. MD simulations showing the microscopic structural feature of the DPIC. (**a**) The coarse-grained MD simulations of the DPIC formation for a system containing 7 random dsDNAs and 27 p53^{4M} ΔTAD tetramers at the temperature of 300 K and the salt concentration of 150 mM. (i) The coarse-grained model of p53^{4M} ΔTAD tetramer and dsDNA chain. The DBD and CTD of p53 were colored by cyan and green, respectively. (ii) A representative structure showing the protein-DNA network formed after 1× 10^8 steps of MD simulations. (**b**) Representative structures from the MD simulation snapshots with

the $p53^{4M}$ ΔTAD tetramer bound with one dsDNA (N_{DNA} = 1), two dsDNAs (N_{DNA} = 2), three dsDNAs (N_{DNA} = 3), and four dsDNAs (N_{DNA} = 4), respectively. The simulations were performed with the similar conditions as (a) but for a smaller system containing 2 $p53^{4M}$ ΔTAD tetramers and 10 dsDNA chains (MD 1). (**c**) Probability distribution of the number of bound 199-bp dsDNA (N_{DNA}) for each $p53^{4M}$ ΔTAD tetramer (MD 1: blue) or full length $p53^{4M}$ (MD 2: green) at a temperature of 300 K and a salt concentration of 150 mM. (**d**) Probability distribution of the number of bound 199-bp dsDNA for each $p53^{4M}$ ΔTAD tetramer at a temperature of 300 K and a salt concentration of 150 mM (MD 1: blue) or 250 mM (MD 3: orange). (**e**) The average *Lifetime* of binding between p53 core DBD and DNA duplex from MD 1 and 3. The probabilities and average *Lifetime* were calculated based on the snapshots from three independent MD simulations (n = 3). The snapshots of the first 3×10^7 MD steps were omitted in calculating the probability distribution of N_{DNA}. Error bars, mean ± s.d.

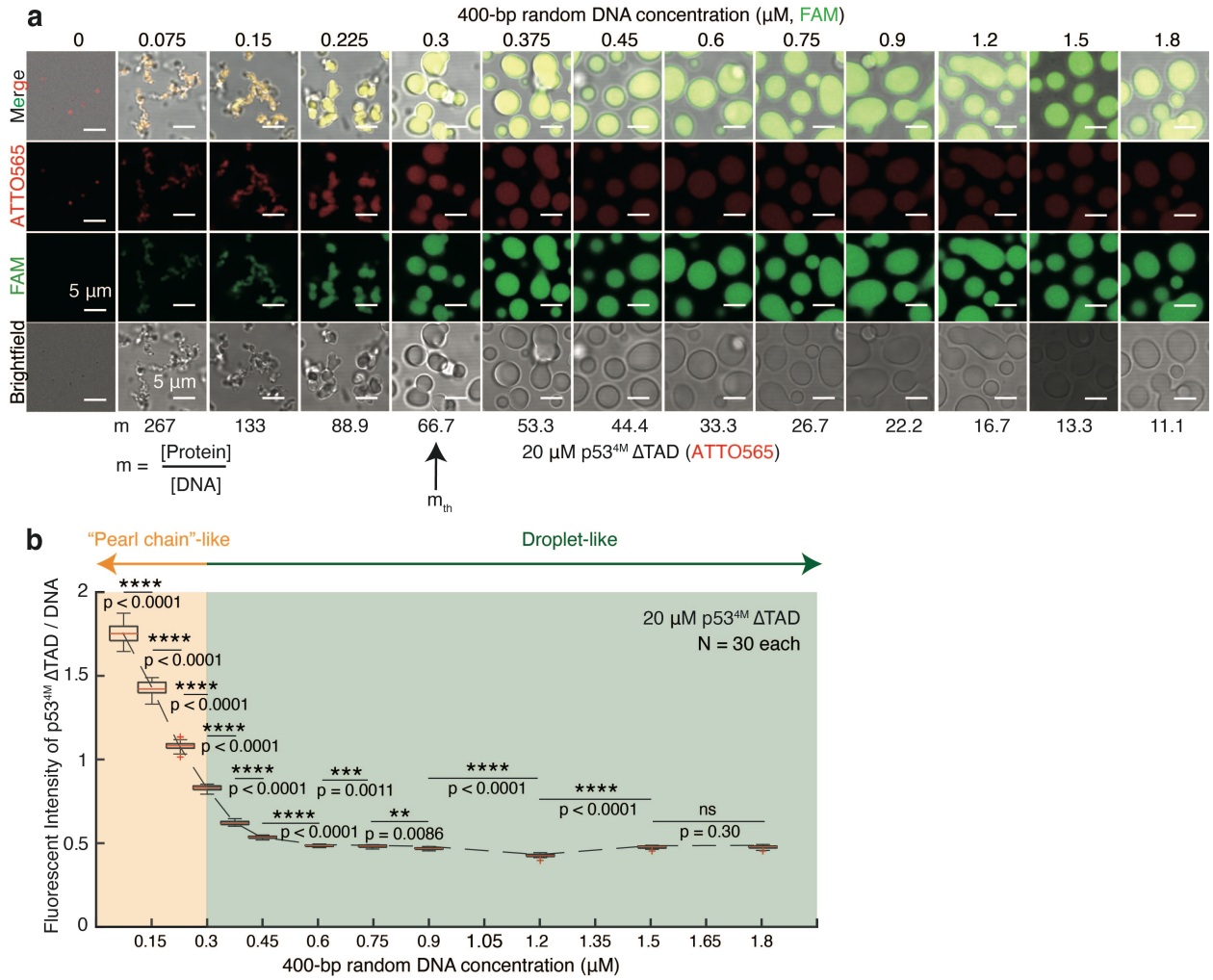

Fig. 3. Morphology transition from droplet-like to "pearl chain"-like DPICs induced by increasing the number of bridges on each DNA. (**a**) Two-color *in vitro* droplet assays involving the mixing of 0, 0.075, 0.15, 0.225, 0.3, 0.375, 0.45, 0.6, 0.75, 0.9, 1.2, 1.5, and 1.8 μM 400-bp random DNA labeled by FAM with 20 μM p53^{4M} ΔTAD labeled by ATTO565. The initial molar ratio between p53 and DNA for each condition (m value) is provided. Independent *in vitro* droplet experiments were conducted three times (n = 3). (**b**) Boxplot of intensity ratio of p53^{4M} ΔTAD / DNA within DPIC for all conditions in a. The total number (N) of DPICs examined for each condition was 30. For the boxplot, the red bar represents median. The bottom edge of the box represents 25th percentiles, and the

top is 75th percentiles. Most extreme data points are covered by the whiskers except outliers. The '+' symbol is used to represent the outliers. Statistical significance was analyzed using unpaired t test for two groups. P value: two-tailed; p value style: GP: 0.1234 (ns), 0.0332 (*), 0.0021 (**), 0.0002 (***), <0.0001 (****). Confidence level: 95%.

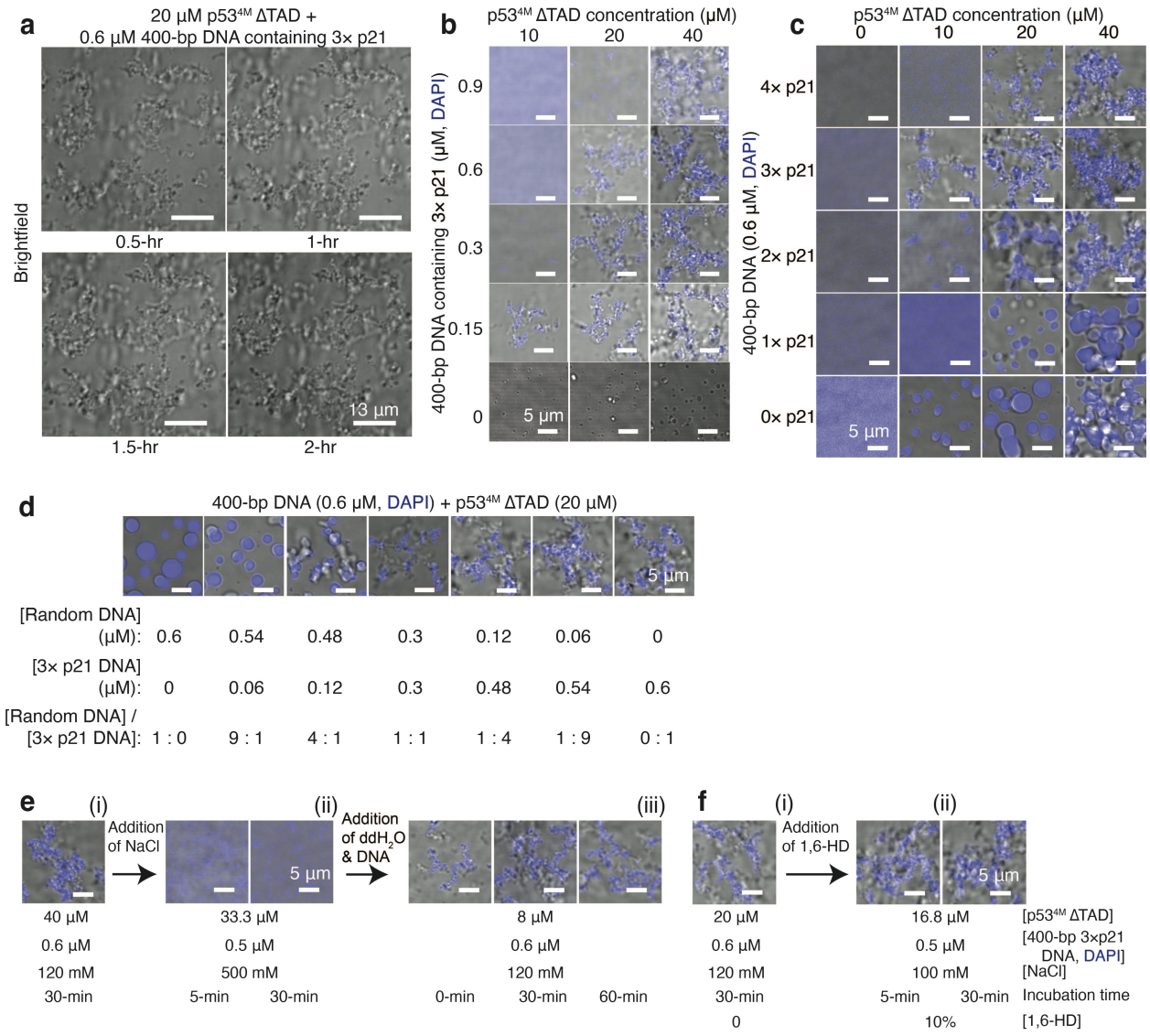

Fig. 4. Morphological transition of DPICs from droplet-like to "pearl chain"-like induced by increasing the total interaction strengths of the system. (**a**) Four panels depicting the time course of fusion events in an *in vitro* droplet experiment with 20 μM p53^{4M} ΔTAD and 0.6 μM 400-bp DNA containing 3× p21 binding motifs (400-bp 3× p21 DNA) (Supplementary Movie 6), with time indicated at the bottom in hours. (**b**) *In vitro* droplet experiments involving the mixing of 0, 0.15, 0.3, 0.6, and 0.9 μM 400-bp DNA containing 3× p21 binding motifs with 10, 20, and 40 μM dark p53^{4M} ΔTAD. (**c**) *In vitro*

droplet experiments by mixing 0.6 μM 400-bp DNA containing 0-4× p21 binding motifs with 0, 10, 20, and 40 μM dark $p53^{4M}$ ΔTAD. (**d**) *In vitro* droplet experiments by mixing 400-bp random DNA and 400-bp DNA containing 3× p21 binding motifs with 20 μM dark $p53^{4M}$ ΔTAD, with changing molar ratios of 400-bp random DNA over 400-bp 3× p21 DNA. (**e**) (i) "Pearl chain"-like DPIC formation with 40 μM $p53^{4M}$ ΔTAD and 0.6 μM 400-bp DNA containing 3× p21 binding motifs under 120 mM NaCl conditions. (ii) Addition of NaCl to 500 mM and incubation for 5 min or 30 min at room temperature (RT). (iii) Addition of extra water and DNA to reduce salt concentration back to 120 mM NaCl and incubation for 0 min, 30 min, or 60 min at RT. (**f**) (i) "Pearl chain"-like DPIC formation with 20 μM $p53^{4M}$ ΔTAD and 0.6 μM 400-bp DNA containing 3× p21 binding motifs under 1,6-HD conditions of 0% 1,6-HD. (ii) Addition of 1,6-HD to 10% and incubation for 5 min or 30 min at RT. DNA was labeled with DAPI. Independent *in vitro* droplet experiments in (a-f) were repeated three times (n = 3) each.

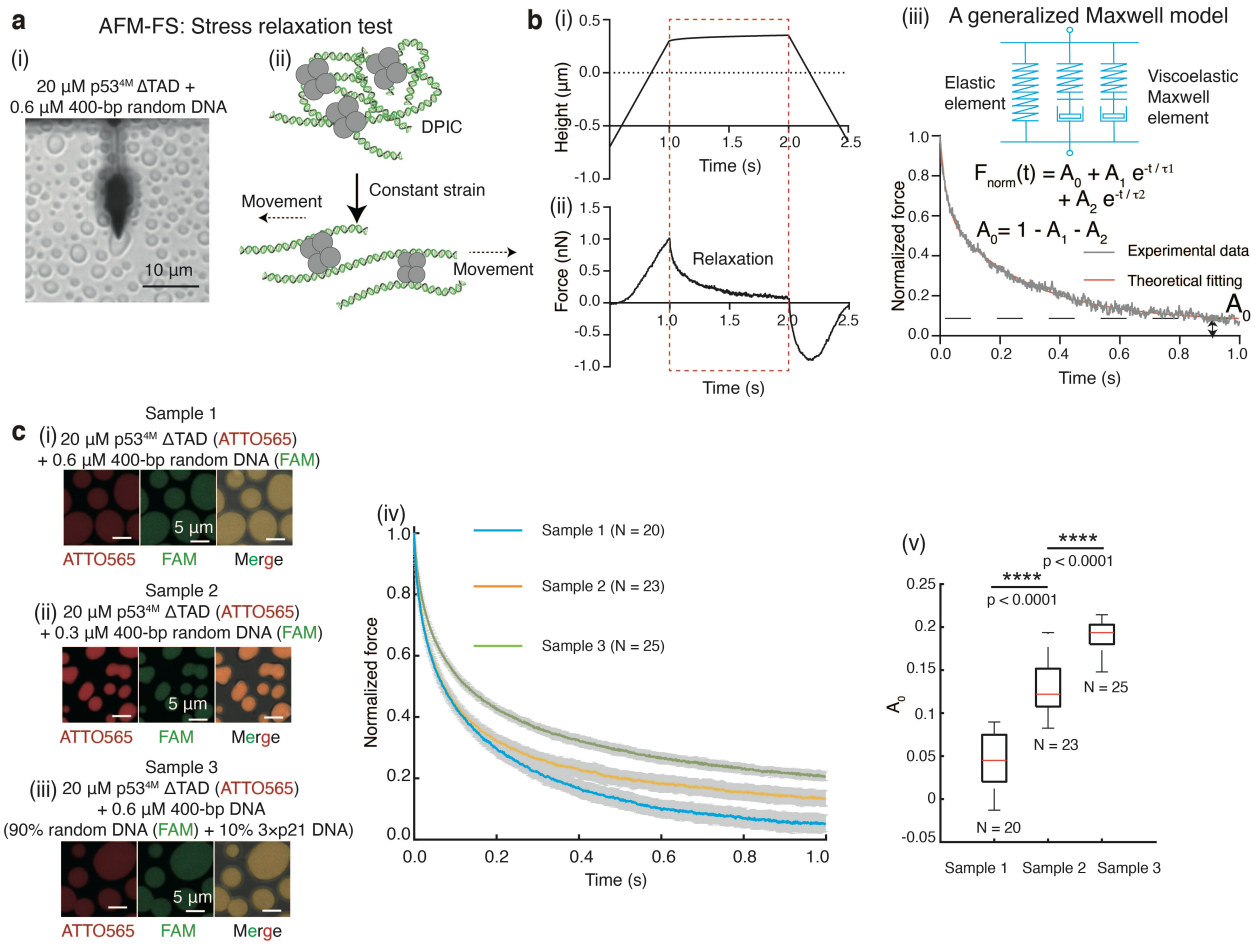

Fig. 5. Characterizing the viscoelastic behavior of DPICs using AFM-FS. (**a**) AFM-FS experiments conducted on the droplet-like DPIC composed of 20 μM p53^{4M} ΔTAD and 0.6 μM 400-bp random DNA. (i) Top-view image of the DPIC under an AFM probe. (ii) Schematic illustration of the stress relaxation test. (**b**) Representative stress relaxation curve of the DPIC. (i) Height-time curve. (ii) Force-time curve. The orange dotted box indicates the relaxation process, where the probe's height remained constant, and the force decreased. (iii) Schematic diagrams of a generalized Maxwell model, comprising one spring and two Maxwell elements in parallel, used for fitting the normalized relaxation curves. (**c**) *In vitro* droplet experiments by combining 20 μM p53^{4M} ΔTAD and 0.6 μM 400-bp random DNA (Sample 1) (i), 20 μM p53^{4M} ΔTAD and 0.3 μM 400-bp random DNA

(Sample 2) (ii), and 20 μM $p53^{4M}$ ΔTAD and 400-bp DNA containing 90% 400-bp random DNA and 10% 400-bp DNA containing 3× p21 binding motif (Sample 3) (iii). $p53^{4M}$ ΔTAD was labeled with ATTO565, and 400-bp DNA was labeled with FAM. DPICs were incubated for 1 hour at room temperature. (iv) Normalized relaxation curves of the DPICs: Sample 1, blue; Sample 2, orange; Sample 3, green. The colored line represents the mean value, and the gray area represents s.d. (v) Boxplot of A_0 for the three samples in c(i). The total number (N) of DPICs examined in a single AFM-FS experiment: N = 20 for Sample 1; N = 23 for Sample 2; N = 25 for Sample 3. For the boxplot, the red bar represents median. The bottom edge of the box represents 25th percentiles, and the top is 75th percentiles. Most extreme data points are covered by the whiskers except outliers. The '+' symbol is used to represent the outliers. Statistical significance was analyzed using unpaired t test for two groups. P value: two-tailed; p value style: GP: 0.1234 (ns), 0.0332 (*), 0.0021 (**), 0.0002 (***), <0.0001 (****). Confidence level: 95%.

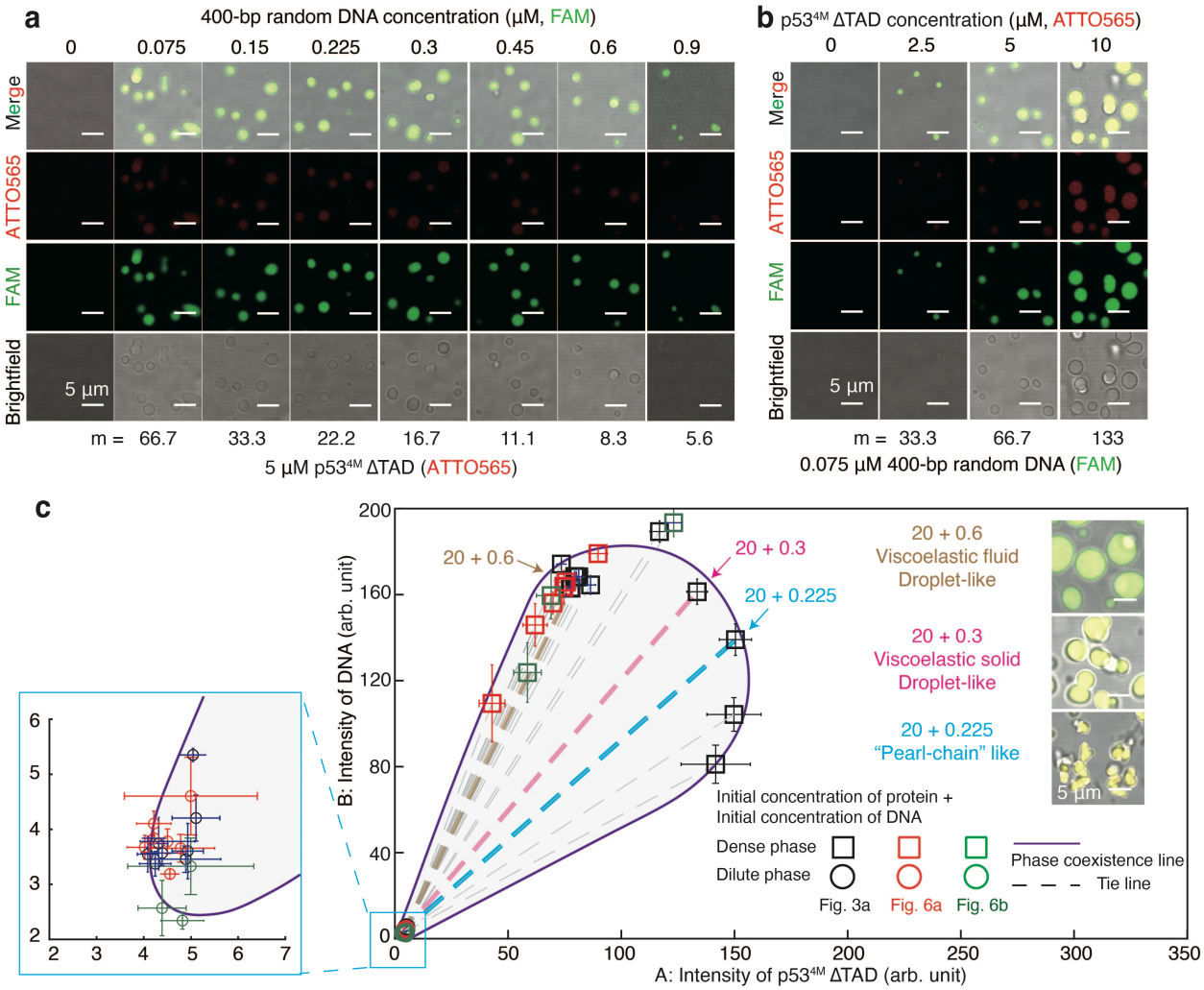

Fig. 6. Two types of transitions in the two-component phase diagram of DPICs. (**a**) Two-color *in vitro* droplet assays were conducted by combining 0, 0.075, 0.15, 0.225, 0.3, 0.45, 0.6, and 0.9 μM 400-bp random DNA labeled with FAM with 5 μM p53^{4M} ΔTAD labeled with ATTO565. (**b**) Two-color *in vitro* droplet assays involved mixing 0, 2.5, 5, and 10 μM p53^{4M} ΔTAD labeled with ATTO565 with 0.075 μM 400-bp random DNA labeled with FAM. The working buffer for *in vitro* droplet assays comprised 8 mM Tris-HCl (pH 7.5), 120 mM NaCl, 4% Glycerol, and 16 mM DTT. Independent *in vitro* droplet experiments were performed three times (n = 3). (**c**) Two-component phase diagram of DPIC. The intensity of p53^{4M} ΔTAD (ATTO565) and 400-bp random DNA (FAM) in both

the dense (square) and dilute phases (circle) from all conditions in Fig. 3a (black), 6a (red), and 6b (green) were plotted. The box zooms in on all data points in the dilute phase. The numbers labeling the dense or dilute phase represent the initial concentration of $p53^{4M}$ ΔTAD and the initial concentration of 400-bp random DNA. The dashed line connecting data points of the dense phase and dilute phase for each condition represents the tie line.

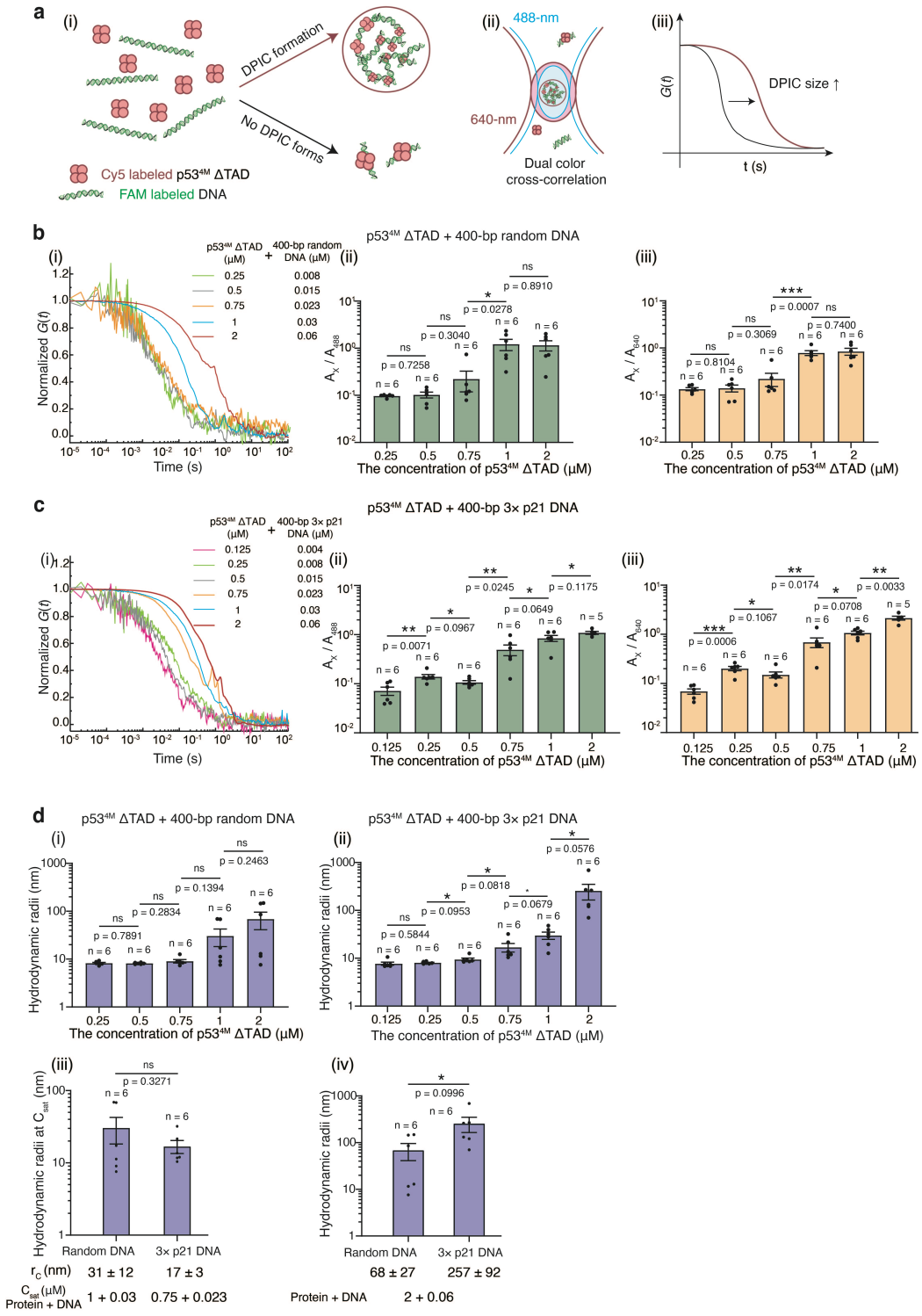

Fig. 7. Droplet-like and "pearl chain"-like DPICs can form similar nm-sized CMCs. (**a**) Schematic diagram of the dcFCCS assay. (i)-(ii) p53^{4M} ΔTAD labeled with Cy5 and 400-bp DNA labeled with FAM (i) diffuse freely through the detection volumes of 488- and

640-nm lasers (ii). (iii) Only the heterocomplexes carrying both Cy5-labeled protein and FAM-labeled DNA contribute to cross-correlation curves, with relaxation times correlating to their size. (**b-c**) dcFCCS analysis of conditions involving the mixing of $p53^{4M}$ ΔTAD and 400-bp DNA. (i) Representative normalized dcFCCS curves for mixtures of Cy5-labeled $p53^{4M}$ ΔTAD and FAM-labeled 400-bp DNA, with listed concentrations of protein and DNA. (ii) and (iii) A_X / A_{488} and A_X / A_{640} indicate the participation ratios of $p53^{4M}$ ΔTAD and 400-bp DNA, respectively, in the protein-DNA heterocomplexes. 400-bp random DNA (b) and 400-bp DNA containing 3× p21 binding motifs (3× p21 DNA) (c). (**d**) Hydrodynamic radii of heterocomplexes formed by $p53^{4M}$ ΔTAD and (i) 400-bp random DNA or (ii) 400-bp 3× p21 DNA. (iii) The hydrodynamic radii of heterocomplexes containing these two types of DNA substrates under C_{sat} conditions, estimating the size of CMC of DPICs (r_c). (iv) The hydrodynamic radii of heterocomplexes containing these two types of DNA substrates under the condition composed of 2 μM $p53^{4M}$ ΔTAD and 0.06 μM DNA. The working buffer for dcFCCS assays was 8 mM Tris-HCl (pH 7.5), 120 mM NaCl, and 16 mM DTT. Independent dcFCCS assays were performed more than 5 times for each condition. Error bars in Fig. 5b, c, d, represent mean ± s.e.m. Statistical significance was analyzed using unpaired t test for two groups. P value: two-tailed; p value style: GP: 0.1234 (ns), 0.0332 (*), 0.0021 (**), 0.0002 (***), <0.0001 (****). Confidence level: 95%.

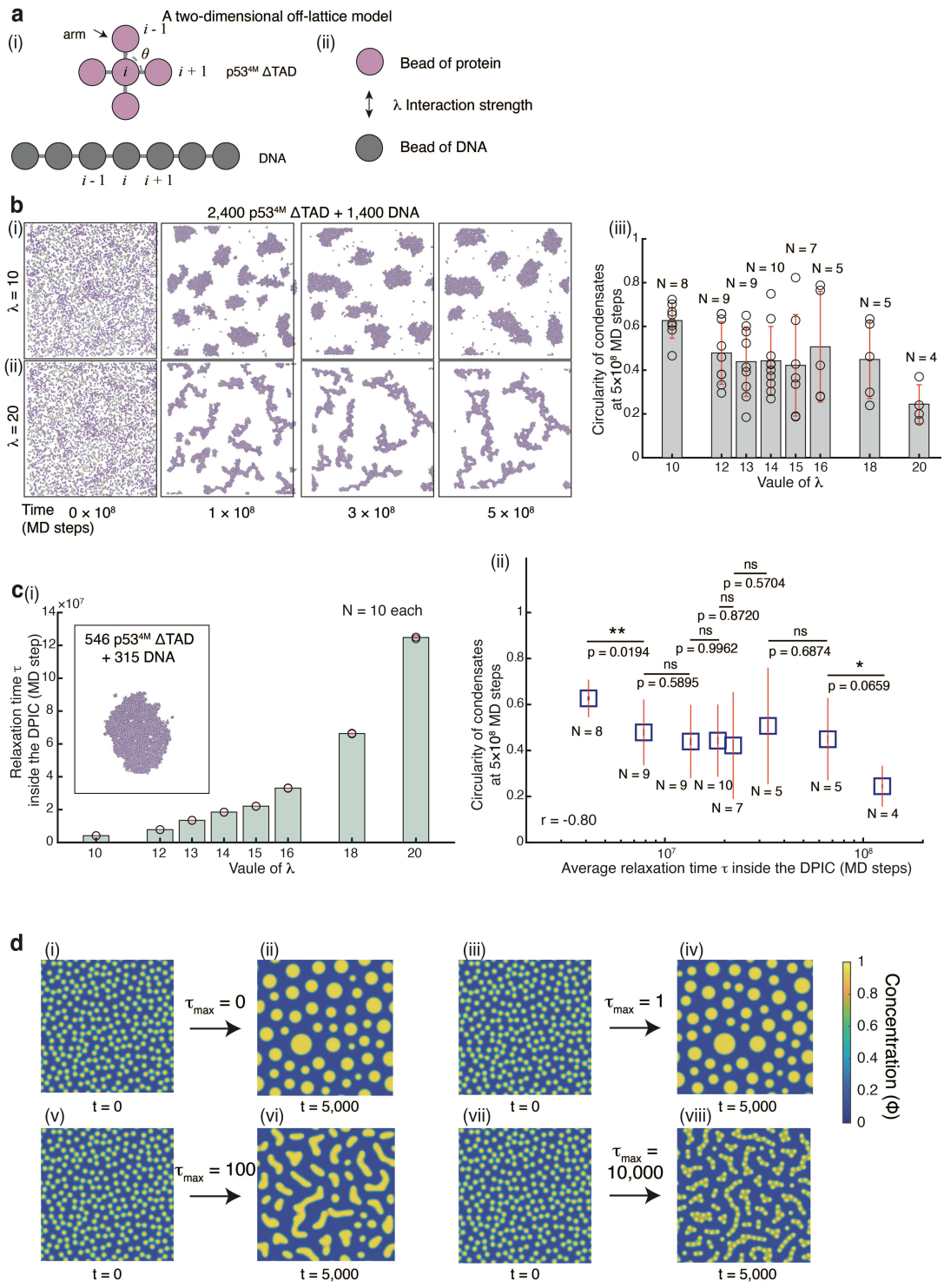

Fig. 8. Interplay between relaxation time and morphology: simulations with a two-dimensional off-lattice model and a mathematical model based on VPS theory. (a) Schematic illustration of the two-dimensional off-lattice model. (i) Simplified structure of

p53 tetramer and dsDNA. (ii) The interaction strength between the branching bead of $p53^{4M}$ ΔTAD tetramer and the bead on DNA was controlled by a parameter λ. (**b**) DPIC formation in the simulation system containing 2,400 $p53^{4M}$ ΔTAD tetramers and 1,400 DNA chains with λ = 10 (i) or λ = 20 (ii). The circularity of DPICs formed after 5×10^8 steps of simulations with different λ was shown in (iii). The total number of DPICs (N) formed in each simulation and used for the calculation of the circularity was listed. (**c**) Dynamic property of DPICs with different λ. (i) The value of relaxation time calculated from the diffusion coefficient in Supplementary Fig. 8. We used 10 snapshots from the diffusion simulations to extract the droplet radius in estimating the relaxation time. The box shows the starting structure of the condensate containing 546 $p53^{4M}$ ΔTAD and 315 DNA chains. (ii) Correlation between estimated relaxation time and DPIC circularity given in 8b(iii) and 8c(i). Error bars in b and c represent mean ± s.d. Statistical significance was analyzed using unpaired t test for two groups. P value: two-tailed; p value style: GP: 0.1234 (ns), 0.0332 (*), 0.0021 (**), 0.0002 (***), <0.0001 (****). Confidence level: 95%. (**d**) Results by a mathematical model based on the VPS theory. Droplets with the same size were randomly placed in a square box at the initial state (i. iii, v, and vii), then underwent coalescence after 5,000 steps with τ_{max} = 0 (ii), τ_{max} = 1 (iv), τ_{max} = 100 (vi), and τ_{max} = 10,000 (viii). The color represented the concentration of substrates (ϕ).

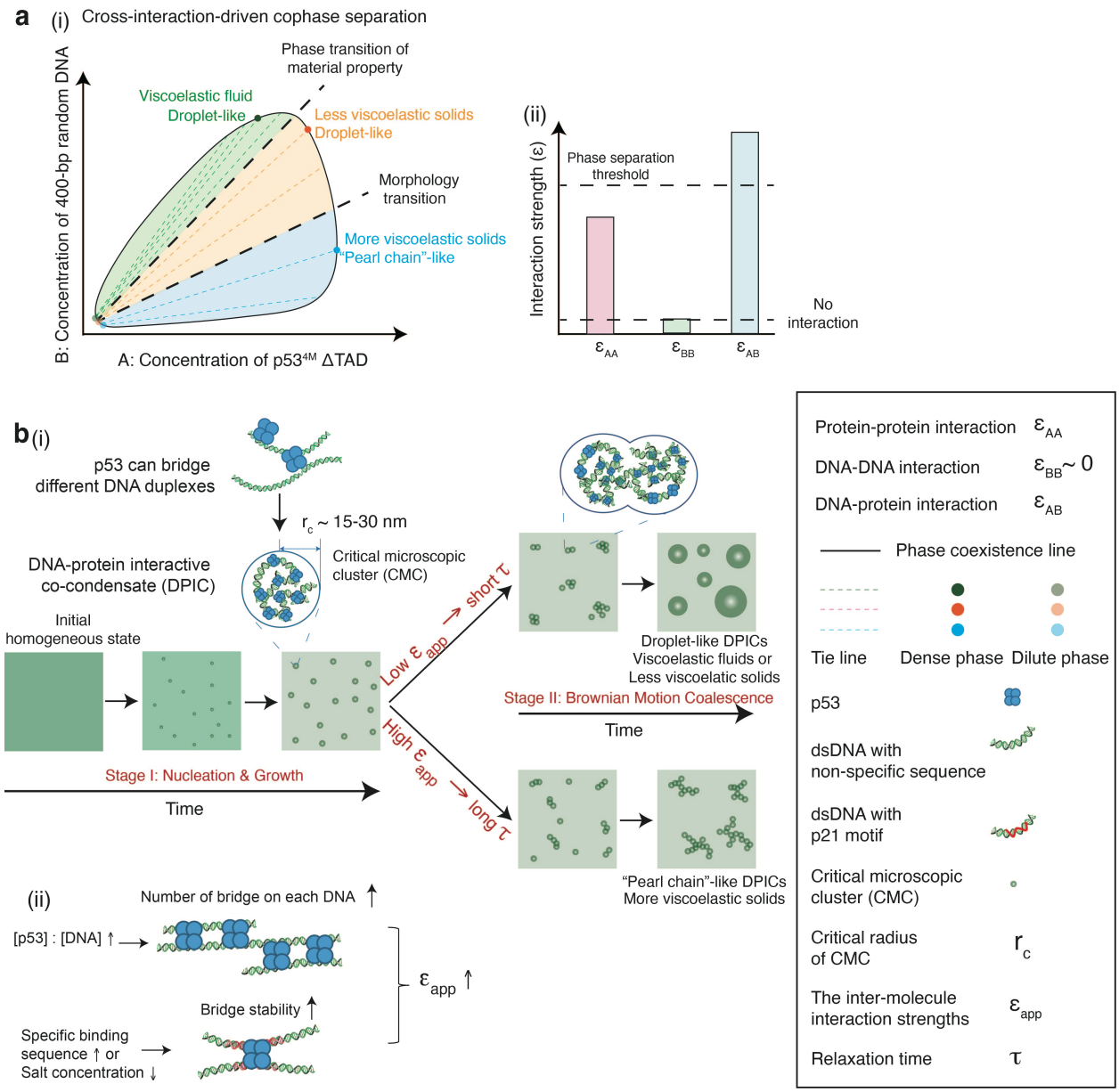

Fig. 9. Theoretical model illustrating the molecular mechanism of DPICs. (**a**) (i) Schematic illustration of the two-component phase diagram of DPIC; (ii) Schematic illustration of the inter-molecular interaction strengths in DPICs. (**b**) (i) We propose a model based on established principles in soft matter physics concerning nucleation, growth, and coarsening; (ii) Schematic illustration showing that increasing the number of bridges on each DNA or the binding affinity between DNA and protein can increase ε_{app}.

Methods

Construction of bacterial expression plasmids

It has been previously proved (Nikolova *et al.*, 1998) that four mutations (M133L/V203A/N239Y/N268D) on wild type (WT) human p53 could make the protein stable *in vitro*. We cloned full-length p53 on pRSFDuet vector, mutated those bases and introduced His-tag to construct the plasmid (No. 1) – 6×His-p53^{4M}. From N-terminal to C-terminal, p53^{4M} can be divided into following domains: NTD (1-94), DBD (95-292), TET (293-356) and CTD (357-393). NTD and CTD are N-terminal domain and C-terminal domain, DBD is the middle core domain that is also DNA binding domain, and TET is the tetramerization domain. NTD includes two TADs (tandem transcription activation domain) and one PRD (Proline-rich domain). We deleted the TAD1 and TAD2 to get a new plasmid (No. 2) – 6×His-PRD-DBD-TET-CTD (p53^{4M} ΔTAD). Protein sequences were shown in the excel below.

Protein purification and labeling

The expression plasmids for all proteins above were transformed into *E. coli* strain BL21(DE3), and then cultured overnight on LB agar plates. A single clone obtained from the plate was cultured in 10 mL LB medium overnight at 37 °C and 220 rpm with 50 μg/mL Kanamycin. The culture was diluted by 1:250 into 2 L LB medium, and then grew to a density (OD600 nm) of 0.6. Bacteria were induced with 0.3 mM IPTG and 0.1 mM $ZnCl_2$ at 16 ^{o}C and 180 rpm overnight. Cultures were centrifuged with 4,000 g. Cells were resuspended in a lysis buffer (25 mM Tris-HCl (pH 7.5), 500 mM NaCl, 5 mM imidazole, 0.25‰ β-Mercaptoethanol (β-Me), and 5% Glycerol), and then sonicated with 1 mM

PMSF on ice. Supernatant was collected and filtered after centrifugation at 18,000 rpm for 40 minutes. Ni-NTA was used to bind p53, and the beads were washed by a washing buffer (25 mM Tris-HCl (pH 7.5), 500 mM NaCl, 20 mM imidazole, 0.25‰ β-Me, and 5% Glycerol). Finally, the protein was eluted by an elution buffer (25 mM Tris-HCl (pH 7.5), 500 mM NaCl, 300 mM imidazole, 0.25‰ β-Me, and 5% Glycerol), and stored at -80 ^{o}C in a storage buffer (20 mM Tris-HCl (pH 7.5), 300 mM NaCl, 10% Glycerol, and 40 mM DTT) after further purification by gel filtration with a Superdex 200 increase GL 10/300 (GE Healthcare, USA). Purified proteins were checked by SDS-PAGE.

In the FRAP assay, $p53^{4M}$ ΔTAD was labeled by ATTO565 NHS ester (Sigma Cat: 72464) at 1:1.5 molar ratios in 0.1 M $NaHCO_3$ for 1 hour at 4 ^{o}C. In the dcFCCS assay, $p53^{4M}$ ΔTAD was labeled by Sulfo Cyanine5 (Cy5) NHS ester (Lumiprobe) at 1:4 molar ratios in reaction buffer (20 mM HEPES pH 7.5, 150 mM KCl, 10% glycerol, 1 mM TCEP) and incubated for 20 min at RT. After labeling, the labeled protein molecules were separated from the free dye and changed into storage buffer (20 mM Tris-HCl (pH 7.5), 300 mM NaCl, 10% Glycerol, and 40 mM DTT) on the Superdex 200 increase GL 10/300. Then labeled protein samples were stored at -80 ^{o}C.

Electrophoretic Mobility Shift Assay (EMSA)

<u>EMSA</u>

EMSA has been performed to test the binding affinity of proteins used in this paper on DNA. 199-bp DNA probe with or without p53 specific binding site was amplified from plasmid by PCR with one primer labeled by 5'-quasar 670 and prepared at a final concentration of 500nM in ddH_2O. The DNA sequences are shown in the excel below.

The DNA binding reaction was performed with a DNA probe of 5 nM final concentration in the p53 working buffer (20 mM HEPES (pH 7.9), 150 mM NaCl, 2 mM $MgCl_2$, 1 mM DTT, and 0.5 mg/mL BSA). $p53^{4M}$ or truncated version protein was serial diluted and mixed with DNA probe at different working concentration. DNA-protein mixture was incubated for 30 minutes at room temperature (RT) and resolved by 1% agarose gel in TBE buffer under 80 V for 80 minutes in cold room (4 °C). The results of EMSA are identified from scanning through the Cy5 channel by Amersham Typhoon.

In vitro **droplet assay**

In vitro droplet assays

All *in vitro* samples were dropped into 384-well plates (Cellvis). If not mentioned, the p53 droplet buffer was 8 mM Tris-HCl (pH 7.5), 120 mM NaCl, 4% Glycerol, and 16 mM DTT. The salt concentration was changed in different experiments. The $p53^{4M}$ or truncated version protein and DNA with different length or sequence are centrifuged at 12,000× g for 10 min at 4 °C before usage, and then diluted to different working concentration by storage buffer or ddH_2O. The DNA-protein mixture is incubated at room temperature (RT) for 0.5 hour. Confocal (Leica TCS SP8) was used to observe DPIC.

Fluorescence recovery after photobleaching (FRAP)

For the FRAP experiment, the DNA-protein mixture was incubated at RT for 2 hours to obtain sufficiently large droplet-like condensates. We used a spinning-disk confocal microscopy (UltraView VoX) to bleach an area of 1.5 μm × 1.5 μm inside each droplet by 488 nm and 561 nm laser with strength of 100% for 30 cycles, and recorded the recovery process with a speed of 2 minutes per frame for 120 minutes. With the program described

above, we obtained a chronological series of photos, and analyzed fluorescence intensity of the bleached regions together with controlled ones to normalize and plot a curve (Supplementary Fig 3).

Fluorescence intensity measurement of protein and DNA inside DPIC

The DPICs formed by ATTO565 labeled $p53^{4M}$ ΔTAD and FAM labeled 400-bp random DNA were incubated at RT for 30 min, and then scanned by 488- and 552-nm lasers on Leica TCS SP8 microscope. The laser strength and the gain value of detectors were fixed during observation. Images were analyzed with Fiji (ImageJ Version: 2.0.0-rc-61/1.52n). The image in fluorescent channel was first adjusted to 8-bit. For each field of observation, 10 DPICs were selected, and the average fluorescence intensity per pixel inside them was measured in ATTO565 channel and FAM channel, respectively. Three independent fields of view were measured for each experimental condition.

Droplet circularity analysis

To obtain the circularity of condensates, the image in fluorescent channel was first adjusted to 8-bit. Threshold of the image was automatically set to identify particles with the subroutine of “threshold” in Fiji (Image/Adjust/Threshold). Particles larger than 1 μm^2 were selected for shape descriptors analysis with the subroutine of “analyze particles” in Fiji (Analyze/Analyze particles). The average circularity can be calculated from all measured values.

To measure the circularity of DPICs formed by the two-dimensional off-lattice model, the snapshots of all condensates at 5×10^8 MD steps were first binarized with the subroutine of “Make binary” in Fiji (Process/Binary/Make binary). To reduce the effect of rough boundaries caused by simplified structure of p53 tetramer and dsDNA, the images

were undergo smoothed with the subroutine of “Smooth” in Fiji (Process/Smooth). Threshold of the images was set automatically, and the condensates larger than 100 pixels were measured.

Dual-color Fluorescence Cross-correlation Spectroscopy (dcFCCS)

The dcFCCS measurements were performed by a home-made confocal microscope with 488- and 640-nm lasers. More details about the setup of microscope can be referred to the previous procedure (Peng *et al.*, 2020). Powers of lasers were set about 5 μW after the objective. The laser focus was 10 μm above the coverslip-water interface. The temperature was 25 ^{o}C. In all dcFCCS measurements, the working buffer was 8 mM Tris-HCl (pH 7.5), 120 mM NaCl, and 16 mM DTT. It took 5 min to mix protein and DNA well, to load them into the reaction chamber, to turn on laser and detectors, and to start collecting data. Raw data of photon arriving time of FAM detection channel (ET525/50m, Chroma) and Cy5 detection channel (ET700/75m, Chroma) was recorded for 5 min. For each experimental condition, at least 5 repeats were performed. Auto-correlation curves of FAM detection channel and Cy5 detection channel and cross-correlation curve between them were calculated from the raw photon arriving time using a home-made MATLAB script.

Atomic Force Microscopy-based Force Spectroscopy (AFM-FS)

For AFM-FS experiments, all DPIC samples were incubated at RT for 1 hour and washed by the droplet buffer, removing all DPICs which cannot adhere tightly to the coverslip surface. Measurements were performed with the operation mode of force volume mode

in fluid on the commercial AFM BioScope Resolve (Bruker, Billerica, MA, USA). A silicon nitride probe (PFQNM-LC-A-CAL, Bruker) with a tip height of 17 μm, a tip radius of 70 nm, and pre-calibrated spring constant of 0.076 N/m was used for the force measurements. All the force curves were recorded with the loading and unloading speed of 2 μm/s, scan size of 50 nm, ramps/line of 4, ramp size of 2 μm, ramp rate of 0.5 Hz, and the deflection error triggers a threshold of 13 nm. For the stress relaxation test, the tip was hold at a fixed height above the DPIC for 1 second by using the hold type of Z-drive after the deflection error trigger threshold was reached. The sampling rate is 1,024 Hz. All experiments were done at RT within 1 hour. Each DPIC was indented for 16 times and about 20 different DPICs were tested for each condition.

All AFM results were imported into the Nanoscope Analysis software (Bruker). For each DPIC, according to whether the force baselines of extend or retract overlap, three sets of force curves (n = 3) with good overlap were picked from 16 sets of stress relaxation test manually. The values of force baseline of picked curves were then corrected to 0 through the Baseline correction of the software with 0th correction order. The force-time, height-time and separation-time curves of each DPIC were derived. The force-time curves were then imported into the Excel software. The time range of the hold process was picked out. To calculate the normalized force, the force value of each time point was divided by the maximum value during the hold process.

Unpaired t test

Statistical significance was evaluated based on Student's t-tests (Prism 9 for macOS, Version 9.1.0 (216), March 15, 2021, GraphPad Software, Inc.). Test was chosen as

unpaired t test. P value style: GP: 0.1234 (ns), 0.0332 (*), 0.0021 (**), 0.0002 (***), < 0.0001 (****).

Box-plot

The function of “boxplot” in MATLAB software (R2015a, 64-bit, February 12, 2015) was used to plot the boxplots in Fig. 3, 5, and Supplementary Fig. 6 and 9. For each boxplot, the red bar represents median. The bottom edge of the box represents 25th percentiles, and the top is 75th percentiles. Most extreme data points are covered by the whiskers except outliers. The '+' symbol is used to represent the outliers.

References

Alberti, S. (2017). Phase separation in biology. Current Biology *27*, R1097-R1102. DOI 10.1016/j.cub.2017.08.069.

Alberti, S., and Dormann, D. (2019). Liquid-Liquid Phase Separation in Disease. Annual Review of Genetics, Vol 53 *53*, 171-194. 10.1146/annurev-genet-112618-043527.

Alberti, S., Gladfelter, A., and Mittag, T. (2019). Considerations and Challenges in Studying Liquid-Liquid Phase Separation and Biomolecular Condensates. Cell *176*, 419-434. 10.1016/j.cell.2018.12.035.

Alshareedah, I., Kaur, T., Ngo, J., Seppala, H., Kounatse, L.A.D., Wang, W., Moosa, M.M., and Banerjee, P.R. (2019). Interplay between Short-Range Attraction and Long-Range Repulsion Controls Reentrant Liquid Condensation of Ribonucleoprotein-RNA Complexes. J Am Chem Soc *141*, 14593-14602. 10.1021/jacs.9b03689.

Alshareedah, I., Moosa, M.M., Pham, M., Potoyan, D.A., and Banerjee, P.R. (2021). Programmable viscoelasticity in protein-RNA condensates with disordered sticker-spacer polypeptides. Nature Communications *12*, 6620. 10.1038/s41467-021-26733-7.

Alshareedah, I., Singh, A., Quinn, A., and Banerjee, P.R. (2022). Determinants of Viscoelasticity and Flow Activation Energy in Biomolecular Condensates. bioRxiv, 2022.2012.2030.522262. 10.1101/2022.12.30.522262.

Banani, S.F., Lee, H.O., Hyman, A.A., and Rosen, M.K. (2017). Biomolecular condensates: organizers of cellular biochemistry. Nat Rev Mol Cell Bio *18*, 285-298. 10.1038/nrm.2017.7.

Berry, J., Brangwynne, C.P., and Haataja, M. (2018). Physical principles of intracellular organization via active and passive phase transitions. Reports on Progress in Physics *80*. ARTN 046601 10.1088/1361-6633/aaa61e.

Boeynaems, S., Alberti, S., Fawzi, N.L., Mittag, T., Polymenidou, M., Rousseau, F., Schymkowitz, J., Shorter, J., Wolozin, B., Van den Bosch, L., et al. (2018). Protein Phase Separation: A New Phase in Cell Biology. Trends in Cell Biology *28*, 420-435. 10.1016/j.tcb.2018.02.004.

Boeynaems, S., Holehouse, A.S., Weinhardt, V., Kovacs, D., Van Lindt, J., Larabell, C., Van Den Bosch, L., Das, R., Tompa, P.S., Pappu, R.V., and Gitler, A.D. (2019). Spontaneous driving forces give rise to protein-RNA condensates with coexisting phases and complex material properties. P Natl Acad Sci USA *116*, 7889-7898. 10.1073/pnas.1821038116.

Boija, A., Klein, I.A., Sabari, B.R., Dall'Agnese, A., Coffey, E.L., Zamudio, A.V., Li, C.H., Shrinivas, K., Manteiga, J.C., Hannett, N.M., et al. (2018). Transcription Factors Activate Genes through the Phase-Separation Capacity of Their Activation Domains. Cell *175*, 1842-+. 10.1016/j.cell.2018.10.042.

Chaudhuri, O., Cooper-White, J., Janmey, P.A., Mooney, D.J., and Shenoy, V.B. (2020). Effects of extracellular matrix viscoelasticity on cellular behaviour. Nature *584*, 535-546. 10.1038/s41586-020-2612-2.

Cho, W.K., Spille, J.H., Hecht, M., Lee, C., Li, C., Grube, V., and Cisse, I.I. (2018). Mediator and RNA polymerase II clusters associate in transcription-dependent condensates. Science *361*, 412-415. 10.1126/science.aar4199.

Chong, S.S., Dugast-Darzacq, C., Liu, Z., Dong, P., Dailey, G.M., Cattoglio, C., Heckert, A., Banala, S., Lavis, L., Darzacq, X., and Tjian, R. (2018). Imaging dynamic and selective low-complexity domain interactions that control gene transcription. Science *361*, 378-+. 10.1126/science.aar2555;eaar2555.

Corominas-Murtra, B., and Petridou, N.I. (2021). Viscoelastic Networks: Forming Cells and Tissues. Front Phys-Lausanne *9*. ARTN 666916 10.3389/fphy.2021.666916.

Dignon, G.L., Best, R.B., and Mittal, J. (2020). Biomolecular Phase Separation: From Molecular Driving Forces to Macroscopic Properties. Annu Rev Phys Chem *71*, 53-75. 10.1146/annurev-physchem-071819-113553.

Dignon, G.L., Zheng, W., Kim, Y.C., Best, R.B., and Mittal, J. (2018). Sequence determinants of protein phase behavior from a coarse-grained model. PLoS Comput Biol *14*, e1005941. 10.1371/journal.pcbi.1005941.

Dorone, Y., Boeynaems, S., Flores, E., Jin, B., Hateley, S., Bossi, F., Lazarus, E., Pennington, J.G., Michiels, E., De Decker, M., et al. (2021). A prion-like protein regulator of seed germination undergoes hydration-dependent phase separation. Cell. https://doi.org/10.1016/j.cell.2021.06.009.

Du, M.J., and Chen, Z.J.J. (2018). DNA-induced liquid phase condensation of cGAS activates innate immune signaling. Science *361*, 704-+. 10.1126/science.aat1022.

Erdel, F., and Rippe, K. (2018). Formation of Chromatin Subcompartments by Phase Separation. Biophys J *114*, 2262-2270. 10.1016/j.bpj.2018.03.011.

Feric, M., and Misteli, T. (2022). Function moves biomolecular condensates in phase space. Bioessays *44*. ARTN e2200001 10.1002/bies.202200001.

Freeman, G.S., Hinckley, D.M., Lequieu, J.P., Whitmer, J.K., and de Pablo, J.J. (2014). Coarse-grained modeling of DNA curvature. J Chem Phys *141*. Artn 165103 10.1063/1.4897649.

Gibson, B.A., Doolittle, L.K., Schneider, M.W.G., Jensen, L.E., Gamarra, N., Henry, L., Gerlich, D.W., Redding, S., and Rosen, M.K. (2019). Organization of Chromatin by Intrinsic and Regulated Phase Separation. Cell *179*, 470-484.e421. https://doi.org/10.1016/j.cell.2019.08.037.

Hafner, A., Bulyk, M.L., Jambhekar, A., and Lahav, G. (2019). The multiple mechanisms that regulate p53 activity and cell fate. Nat Rev Mol Cell Bio *20*, 199-210. 10.1038/s41580-019-0110-x.

Hajime, T. (2000). Viscoelastic phase separation. Journal of Physics: Condensed Matter *12*, R207. 10.1088/0953-8984/12/15/201.

Hansen, J.C., Maeshima, K., and Hendzel, M.J. (2021). The solid and liquid states of chromatin. Epigenetics & Chromatin *14*, 50. 10.1186/s13072-021-00424-5.

Jawerth, L., Fischer-Friedrich, E., Saha, S., Wang, J., Franzmann, T., Zhang, X.J., Sachweh, J., Ruer, M., Ijavi, M., Saha, S., et al. (2020). Protein condensates as aging Maxwell fluids. Science *370*, 1317-+. 10.1126/science.aaw4951.

Jung, J., Mori, T., Kobayashi, C., Matsunaga, Y., Yoda, T., Feig, M., and Sugita, Y. (2015). GENESIS: a hybrid-parallel and multi-scale molecular dynamics simulator with enhanced sampling algorithms for biomolecular and cellular simulations. Wires Comput Mol Sci *5*, 310-323. 10.1002/wcms.1220.

Kapcha, L.H., and Rossky, P.J. (2014). A Simple Atomic-Level Hydrophobicity Scale Reveals Protein Interfacial Structure. J Mol Biol *426*, 484-498. https://doi.org/10.1016/j.jmb.2013.09.039.

Kearns, S., Lurz, R., Orlova, E.V., and Okorokov, A.L. (2016). Two p53 tetramers bind one consensus DNA response element. Nucleic Acids Res *44*, 6185-6199. 10.1093/nar/gkw215.

Kobayashi, C., Jung, J., Matsunaga, Y., Mori, T., Ando, T., Tamura, K., Kamiya, M., and Sugita, Y. (2017). GENESIS 1.1: A hybrid-parallel molecular dynamics simulator with enhanced sampling algorithms on multiple computational platforms. J Comput Chem *38*, 2193-2206. 10.1002/jcc.24874.

Larson, A.G., Elnatan, D., Keenen, M.M., Trnka, M.J., Ohnston, J.B.J., Burlingame, A.L., Agard, D.A., Redding, S., and Narlikar, G.J. (2017). Liquid droplet formation by HP1 alpha suggests a role for phase separation in heterochromatin. Nature *547*, 236-+. 10.1038/nature22822.

Lee, D.S.W., Wingreen, N.S., and Brangwynne, C.P. (2021). Chromatin mechanics dictates subdiffusion and coarsening dynamics of embedded condensates. Nat Phys *17*, 531-+. 10.1038/s41567-020-01125-8.

Lequieu, J., Schwartz, D.C., and de Pablo, J.J. (2017). In silico evidence for sequence-dependent nucleosome sliding. Proceedings of the National Academy of Sciences *114*, E9197-E9205. doi:10.1073/pnas.1705685114.

Li, C.H., Coffey, E.L., Dall'Agnese, A., Hannett, N.M., Tang, X., Henninger, J.E., Platt, J.M., Oksuz, O., Zamudio, A.V., Afeyan, L.K., et al. (2020). MeCP2 links heterochromatin condensates and neurodevelopmental disease. Nature *586*, 440-+. 10.1038/s41586-020-2574-4.

Li, M., Liu, L.Q., Xi, N., and Wang, Y.C. (2018). Atomic force microscopy studies on cellular elastic and viscoelastic properties. Sci China Life Sci *61*, 57-67. 10.1007/s11427-016-9041-9.

Li, P.L., Banjade, S., Cheng, H.C., Kim, S., Chen, B., Guo, L., Llaguno, M., Hollingsworth, J.V., King, D.S., Banani, S.F., et al. (2012). Phase transitions in the assembly of multivalent signalling proteins. Nature *483*, 336-U129. 10.1038/nature10879.

Li, W., Wang, W., and Takada, S. (2014). Energy landscape views for interplays among folding, binding, and allostery of calmodulin domains. Proceedings of the National Academy of Sciences *111*, 10550-10555. doi:10.1073/pnas.1402768111.

Li, W., Wolynes, P.G., and Takada, S. (2011). Frustration, specific sequence dependence, and nonlinearity in large-amplitude fluctuations of allosteric proteins. Proceedings of the National Academy of Sciences *108*, 3504-3509. doi:10.1073/pnas.1018983108.

Lifshitz, I.M., and Slyozov, V.V. (1961). The kinetics of precipitation from supersaturated solid solutions. Journal of Physics and Chemistry of Solids *19*, 35-50. https://doi.org/10.1016/0022-3697(61)90054-3.

Lin, Y., Protter, D.S.W., Rosen, M.K., and Parker, R. (2015). Formation and Maturation of Phase-Separated Liquid Droplets by RNA-Binding Proteins. Mol Cell *60*, 208-219. 10.1016/j.molcel.2015.08.018.

McKinney, K., Mattia, M., Gottifredi, V., and Prives, C. (2004). p53 linear diffusion along DNA requires its C terminus. Mol Cell *16*, 413-424. DOI 10.1016/j.molcel.2004.09.032.

Mittag, T., and Pappu, R.V. (2022). A conceptual framework for understanding phase separation and addressing open questions and challenges. Mol Cell *82*, 2201-2214. https://doi.org/10.1016/j.molcel.2022.05.018.

Molliex, A., Temirov, J., Lee, J., Coughlin, M., Kanagaraj, A.P., Kim, H.J., Mittag, T., and Taylor, J.P. (2015). Phase Separation by Low Complexity Domains Promotes Stress Granule Assembly and Drives Pathological Fibrillization. Cell *163*, 123-133. 10.1016/j.cell.2015.09.015.

Moreno-Flores, S., Benitez, R., Vivanco, M.D., and Toca-Herrera, J.L. (2010a). Stress relaxation and creep on living cells with the atomic force microscope: a means to calculate elastic moduli and viscosities of cell components. Nanotechnology *21*. Artn 445101 10.1088/0957-4484/21/44/445101.

Moreno-Flores, S., Benitez, R., Vivanco, M.D., and Toca-Herrera, J.L. (2010b). Stress relaxation microscopy: Imaging local stress in cells. J Biomech *43*, 349-354. 10.1016/j.jbiomech.2009.07.037.

Nikolova, P.V., Henckel, J., Lane, D.P., and Fersht, A.R. (1998). Semirational design of active tumor suppressor p53 DNA binding domain with enhanced stability. P Natl Acad Sci USA *95*, 14675-14680. DOI 10.1073/pnas.95.25.14675.

Patel, A., Lee, H.O., Jawerth, L., Maharana, S., Jahnel, M., Hein, M.Y., Stoynov, S., Mahamid, J., Saha, S., Franzmann, T.M., et al. (2015). A Liquid-to-Solid Phase Transition of the ALS Protein FUS Accelerated by Disease Mutation. Cell *162*, 1066-1077. 10.1016/j.cell.2015.07.047.

Peng, S.J., Li, W.P., Yao, Y.R., Xing, W.J., Li, P.L., and Chen, C.L. (2020). Phase separation at the nanoscale quantified by dcFCCS. P Natl Acad Sci USA *117*, 27124-27131. 10.1073/pnas.2008447117.

Quail, T., Golfier, S., Elsner, M., Ishihara, K., Murugesan, V., Renger, R., Julicher, F., and Brugues, J. (2021). Force generation by protein-DNA co-condensation. Nat Phys *17*, 1007-+. 10.1038/s41567-021-01285-1.

Ryu, J.K., Bouchoux, C., Liu, H.W., Kim, E., Minamino, M., de Groot, R., Katan, A.J., Bonato, A., Marenduzzo, D., Michieletto, D., et al. (2021). Bridging-induced phase separation induced by cohesin SMC protein complexes. Sci Adv *7*. ARTN eabe5905 10.1126/sciadv.abe5905.

Sabari, B.R., Dall'Agnese, A., Boija, A., Klein, I.A., Coffey, E.L., Shrinivas, K., Abraham, B.J., Hannett, N.M., Zamudio, A.V., Manteiga, J.C., et al. (2018). Coactivator condensation at super-enhancers links phase separation and gene control. Science *361*, 379-+. 10.1126/science.aar3958;eaar3958.

Sharma, R., Choi, K.J., Quan, M.D., Sharma, S., Sankaran, B., Park, H., LaGrone, A., Kim, J.J., MacKenzie, K.R., Ferreon, A.C.M., et al. (2021). Liquid condensation of reprogramming factor KLF4 with DNA provides a mechanism for chromatin organization. Nature Communications *12*. ARTN 5579 10.1038/s41467-021-25761-7.

Shin, Y., Berry, J., Pannucci, N., Haataja, M.P., Toettcher, J.E., and Brangwynne, C.P. (2017). Spatiotemporal Control of Intracellular Phase Transitions Using Light-Activated optoDroplets. Cell *168*, 159-+. 10.1016/j.cell.2016.11.054.

Shin, Y., and Brangwynne, C.P. (2017). Liquid phase condensation in cell physiology and disease. Science *357*. ARTN eaaf4382 10.1126/science.aaf4382.

Strickfaden, H., Tolsma, T.O., Sharma, A., Underhill, D.A., Hansen, J.C., and Hendzel, M.J. (2020). Condensed Chromatin Behaves like a Solid on the Mesoscale In Vitro and in Living Cells. Cell *183*, 1772-+. 10.1016/j.cell.2020.11.027.

Strom, A.R., Emelyanov, A.V., Mir, M., Fyodorov, D.V., Darzacq, X., and Karpen, G.H. (2017). Phase separation drives heterochromatin domain formation. Nature *547*, 241-+. 10.1038/nature22989.

Strom, A.R., Kim, Y., Zhao, H., Orlovsky, N., Chang, Y.-C., Košmrlj, A., Storm, C., and Brangwynne, C.P. (2023). Condensate-driven interfacial forces reposition DNA loci and measure chromatin viscoelasticity. bioRxiv, 2023.2002.2027.530281. 10.1101/2023.02.27.530281.

Sullivan, K.D., Galbraith, M.D., Andrysik, Z., and Espinosa, J.M. (2018). Mechanisms of transcriptional regulation by p53. Cell Death and Differentiation *25*, 133-143. 10.1038/cdd.2017.174.

Tafvizi, A., Huang, F., Fersht, A.R., Mirny, L.A., and van Oijen, A.M. (2011). A single-molecule characterization of p53 search on DNA. P Natl Acad Sci USA *108*, 563-568. 10.1073/pnas.1016020107.

Tan, C., Jung, J.W., Kobayashi, C., La Torre, D.U., Takada, S., and Sugita, Y. (2022). Implementation of residue-level coarse-grained models in GENESIS for large-scale molecular dynamics simulations. Plos Computational Biology *18*. ARTN e1009578 10.1371/journal.pcbi.1009578.

Tan, C., and Takada, S. (2018). Dynamic and Structural Modeling of the Specificity in Protein–DNA Interactions Guided by Binding Assay and Structure Data. Journal of Chemical Theory and Computation *14*, 3877-3889. 10.1021/acs.jctc.8b00299.

Tan, C., and Takada, S. (2020). Nucleosome allostery in pioneer transcription factor binding. Proceedings of the National Academy of Sciences *117*, 20586-20596. doi:10.1073/pnas.2005500117.

Tan, C., Terakawa, T., and Takada, S. (2016). Dynamic Coupling among Protein Binding, Sliding, and DNA Bending Revealed by Molecular Dynamics. J Am Chem Soc *138*, 8512-8522. 10.1021/jacs.6b03729.

Tanaka, H. (2000). Viscoelastic phase separation. J Phys-Condens Mat *12*, R207-R264. Doi 10.1088/0953-8984/12/15/201.

Tanaka, H. (2022). Viscoelastic phase separation in biological cells. Commun Phys-Uk *5*. ARTN 167
10.1038/s42005-022-00947-7.

Tanaka, H., and Araki, T. (2006). Viscoelastic phase separation in soft matter: Numerical-simulation study on its physical mechanism. Chemical Engineering Science *61*, 2108-2141. https://doi.org/10.1016/j.ces.2004.02.025.

Terakawa, T., and Takada, S. (2011). Multiscale Ensemble Modeling of Intrinsically Disordered Proteins: p53 N-Terminal Domain. Biophys J *101*, 1450-1458. https://doi.org/10.1016/j.bpj.2011.08.003.

Uversky, V.N. (2017). Intrinsically disordered proteins in overcrowded milieu: Membrane-less organelles, phase separation, and intrinsic disorder. Current Opinion in Structural Biology *44*, 18-30. 10.1016/j.sbi.2016.10.015.

Vincent, J.F.V. (1982). Basic Theory of Elasticity and Viscoelasticity.

Wang, L., Gao, Y.F., Zheng, X.D., Liu, C.F., Dong, S.S., Li, R., Zhang, G.W., Wei, Y.X., Qu, H.Y., Li, Y.H., et al. (2019). Histone Modifications Regulate Chromatin Compartmentalization by Contributing to a Phase Separation Mechanism. Mol Cell *76*, 646-+. 10.1016/j.molcel.2019.08.019.

Wang, L., Hu, M.L., Zuo, M.Q., Zhao, J.C., Wu, D., Huang, L., Wen, Y.X., Li, Y.F., Chen, P., Bao, X.H., et al. (2020). Rett syndrome-causing mutations compromise MeCP2-mediated liquid-liquid phase separation of chromatin. Cell Res *30*, 393-407. 10.1038/s41422-020-0288-7.

Weber, A., Turri, J.I., Benitez, R., Zemljic-Jokhadar, S., and Oca-Herrera, J.L.T. (2019). Microtubule disruption changes endothelial cell mechanics and adhesion. Sci Rep-Uk *9*. ARTN 14903 10.1038/s41598-019-51024-z.

Wei, C.L., Wu, Q., Vega, V.B., Chiu, K.P., Ng, P., Zhang, T., Shahab, A., Yong, H.C., Fu, Y.T., Weng, Z.P., et al. (2006). A global map of p53 transcription-factor binding sites in the human genome. Cell *124*, 207-219. 10.1016/j.cell.2005.10.043.

Xie, W., Lama, L., Adura, C., Tomita, D., Glickman, J.F., Tuschl, T., and Patel, D.J. (2019). Human cGAS catalytic domain has an additional DNA-binding interface that enhances enzymatic activity and liquid-phase condensation. P Natl Acad Sci USA *116*, 11946-11955. 10.1073/pnas.1905013116.

Xu, G.J., Liu, C., Zhou, S., Li, Q.J., Feng, Y., Sun, P.P., Feng, H., Gao, Y.N., Zhu, J.P., Luo, X., et al. (2021). Viral tegument proteins restrict cGAS-DNA phase separation to mediate immune evasion. Mol Cell *81*, 2823-+. 10.1016/j.molcel.2021.05.002.

Yao, Y., Wang, W., and Chen, C. (2022). Mechanisms of phase-separation-mediated cGAS activation revealed by dcFCCS. PNAS Nexus *1*. 10.1093/pnasnexus/pgac109.

Zhang, H., Elbaum-Garfinkle, S., Langdon, E.M., Taylor, N., Occhipinti, P., Bridges, Andrew A., Brangwynne, Clifford P., and Gladfelter, Amy S. (2015). RNA Controls PolyQ Protein Phase Transitions. Mol Cell *60*, 220-230. 10.1016/j.molcel.2015.09.017.

Zhang, J., Alert, R., Yan, J., Wingreen, N.S., and Granick, S. (2021). Active phase separation by turning towards regions of higher density. Nat Phys *17*, 961-967. 10.1038/s41567-021-01238-8.

Zhou, H., Song, Z., Zhong, S., Zuo, L., Qi, Z., Qu, L.-J., and Lai, L. (2019). Mechanism of DNA-Induced Phase Separation for Transcriptional Repressor VRN1. Angewandte Chemie (International ed. in English) *58*, 4858-4862. 10.1002/anie.201810373.

Zuo, L., Zhang, G., Massett, M., Cheng, J., Guo, Z., Wang, L., Gao, Y., Li, R., Huang, X., Li, P., and Qi, Z. (2021). Loci-specific phase separation of FET fusion oncoproteins promotes gene transcription. Nature Communications *12*, 1491. 10.1038/s41467-021-21690-7.